JGR Planets

Key Points:
- Saturn's northern summertime hemisphere was mapped by JWST/Mid-Infrared Instrument (MIRI) to study seasonal evolution of temperatures, aerosols, and composition
- The data show evidence for changing temperatures and winds in the equatorial oscillation, polar vortices, and interhemispheric stratospheric circulation
- MIRI spectral coverage and sensitivity enables mapping of several gases for the first time, particularly in ranges inaccessible to Cassini

Supporting Information:
Supporting Information may be found in the online version of this article.

Correspondence to:
L. N. Fletcher,
leigh.fletcher@le.ac.uk

Saturn's Atmosphere in Northern Summer Revealed by JWST/MIRI

Leigh N. Fletcher[1] , Oliver R. T. King[1] , Jake Harkett[1], Heidi B. Hammel[2], Michael T. Roman[1] , Henrik Melin[1] , Matthew M. Hedman[3], Julianne I. Moses[4] , Sandrine Guerlet[5,6] , Stefanie N. Milam[7] , and Matthew S. Tiscareno[8]

[1]School of Physics and Astronomy, University of Leicester, Leicester, UK, [2]Association of Universities for Research in Astronomy, Washington, DC, USA, [3]Department of Physics, University of Idaho, Moscow, ID, USA, [4]Space Science Institute, Boulder, CO, USA, [5]Laboratoire de Météorologie Dynamique/Institut Pierre-Simon Laplace (LMD/IPSL), Sorbonne Université, CNRS, École Polytechnique, Institut Polytechnique de Paris, École Normale Supérieure (ENS), PSL Research University, Paris, France, [6]LESIA-Observatoire de Paris, Université PSL, CNRS, Sorbonne Université, University Paris-Diderot, Sorbonne Paris-Cité, Meudon, France, [7]Astrochemistry Laboratory Code 691, NASA Goddard Space Flight Center, Greenbelt, MD, USA, [8]SETI Institute, Mountain View, CA, USA

Abstract Saturn's northern summertime hemisphere was mapped by JWST/Mid-Infrared Instrument (4.9–27.9 μm) in November 2022, tracing the seasonal evolution of temperatures, aerosols, and chemical species in the 5 years since the end of the Cassini mission. The spectral region between reflected sunlight and thermal emission (5.1–6.8 μm) is mapped for the first time, enabling retrievals of phosphine, ammonia, and water, alongside a system of two aerosol layers (an upper tropospheric haze $p < 0.3$ bars, and a deeper cloud layer at 1–2 bars). Ammonia displays substantial equatorial enrichment, suggesting similar dynamical processes to those found in Jupiter's equatorial zone. Saturn's North Polar Stratospheric Vortex has warmed since 2017, entrained by westward winds at $p < 10$ mbar, and exhibits localized enhancements in several hydrocarbons. The strongest latitudinal temperature gradients are co-located with the peaks of the zonal winds, implying wind decay with altitude. Reflectivity contrasts at 5–6 μm compare favorably with albedo contrasts observed by Hubble, and several discrete vortices are observed. A warm equatorial stratospheric band in 2022 is not consistent with a 15-year repeatability for the equatorial oscillation. A stacked system of windshear zones dominates Saturn's equatorial stratosphere, and implies a westward equatorial jet near 1–5 mbar at this epoch. Lower stratospheric temperatures, and local minima in the distributions of several hydrocarbons, imply low-latitude upwelling and a reversal of Saturn's interhemispheric circulation since equinox. Latitudinal distributions of stratospheric ethylene, benzene, methyl, and carbon dioxide are presented for the first time, and we report the first detection of propane bands in the 8–11 μm region.

Plain Language Summary The Saturn system, with its seasonally varying atmosphere, delicate rings, and myriad satellites, presented an ideal early target for JWST. Saturn's extended disc, rapid rotation, and infrared brightness provided a challenge for the small fields-of-view of the Mid-Infrared Instrument (MIRI), requiring a mosaic to map Saturn's northern summertime hemisphere. This exquisite data set reveals Saturn's banded structure, discrete vortices, the warm polar vortices, and the continued evolution of an oscillatory pattern of warm and cool anomalies over Saturn's equator. We show evidence that a stratospheric circulation pattern detected by Cassini during northern winter has now fully reversed in northern summer, with the low-latitude stratosphere being cool and depleted in aerosols due to summertime upwelling. MIRI provides access to spectral regions that were not possible with the Cassini spacecraft, particularly in the 5–7 μm region where reflected sunlight and thermal emission blend together. Ammonia and phosphine are enriched at Saturn's equator, suggesting strong mixing from the deeper troposphere. MIRI's high sensitivity enables the first identification of previously unseen emission propane bands, along with the first measurements of the distribution of several gaseous species: tropospheric water, and stratospheric ethylene, benzene, methyl, and carbon dioxide.

1. Introduction

Spectroscopic mid-infrared observations of the Saturn system by JWST (Gardner et al., 2023) were designed to build on the legacy of discoveries of the Cassini-Huygens mission (2004–2017), exploiting the unprecedented

spectral coverage and sensitivity of the Mid-Infrared Instrument/Medium Resolution Spectrometer (MIRI/MRS) (4.9–27.9 μm, Wright et al., 2023) integral field units (IFUs). As part of a Guaranteed-Time programme for giant planet observations during JWST's first cycle of operations (Fletcher et al., 2021), Saturn provided an ideal test of the capabilities of this new facility. For example, Saturn's large angular size compared to the small fields-of-view of MIRI/MRS presented a challenge for mapping extended, rotating, and moving sources. Saturn's spectrum has a large dynamic range, with some regions (e.g., near 6 μm) sufficiently dark as to require long integrations, but others (e.g., near 25 μm) so bright that they are close to the saturation limit of the sensitive MIRI/MRS detectors. Observations of Saturn's small satellites are challenged by scattered light from Saturn's atmosphere and rings. And given that Saturn's forest of molecular emission and absorption features were previously characterized in detail by Cassini, the Saturn observations provided a sensitive check on the calibration of JWST (e.g., wavelength and flux calibration, and the presence of instrumental artifacts).

In this work, we provide a comprehensive first assessment of JWST mid-infrared observations of Saturn in November 2022 as a baseline for a long-term seasonal legacy for MIRI. The Cassini record of Saturn's seasonal evolution came to an end in 2017 (Fletcher et al., 2020b), shortly after Saturn passed northern summer solstice in May 2017 (planetocentric solar longitude of $L_s = 90°$). Five years later, the northern pole was receding from view during Saturn's mid-summer ($L_s = 150°$) as the planet approached northern autumn equinox in June 2025 ($L_s = 180°$). Cassini-Huygens did not have the opportunity to observe this particular northern-summer season on Saturn, although it was captured one Saturnian year earlier by ground-based imaging observations (e.g., Blake et al., 2022; Orton et al., 2008; Stam et al., 2001) and Hubble observations (Caldwell et al., 1993; Karkoschka & Tomasko, 1993; Westphal et al., 1992) in the early 1990s. The mid-IR observations revealed the cooling of the seasonal North Polar Stratospheric Vortex (NPSV), a region of elevated tropospheric and stratospheric temperatures poleward of 75°N during summer (Fletcher et al., 2018b; Guerlet et al., 2015). Observations in 1993–1995 also captured Saturn's equatorial stratospheric oscillation during its cool equatorial phase (Blake et al., 2022; Orton et al., 2008), which should be replicated in JWST/MIRI observations exactly one Saturnian year later if the oscillation were semi-annual (i.e., a 15-year period, Fouchet et al., 2008; Orton et al., 2008).

The MIRI/MRS instrument brings exceptional new capabilities for infrared science that eluded even the Cassini-Huygens spacecraft. Saturn's 5-μm "window," where deep thermal emission reveals the dynamics and morphology of the cloud-forming region, was extensively mapped by Cassini/VIMS ($R \sim 300$ at 5 μm), but MRS provides an order of magnitude improvement in spectral resolution ($R \sim 3,500$) required to separate gaseous absorption features of phosphine, ammonia, and water; plus it provides spatial mapping of the 5.1–6.9 μm range for the first time (reliable Cassini/CIRS spectroscopy started near 7.0 μm with $R \sim 2,800$). Although this region was previously observed in the disc-averaged sense by ISO (the Short-Wave Spectrometer, with $R \sim 1,000–2,000$, Encrenaz, 2003), the MRS data presented here are the first to spatially map this transitional region between reflected sunlight and thermal emission, revealing discrete features in the cloud deck, and providing access to the spatial distribution of tropospheric water and aerosols, as well as the stratospheric distributions of methane, ethane and other hydrocarbons using previously inaccessible emission bands. Finally, MIRI/MRS provides a dramatic improvement in signal-to-noise in Saturn's 10-μm region, which was plagued by noise in Cassini/CIRS observations (this was the overlap between the two mid-infrared focal plane detectors near 9 μm).

The MIRI/MRS observations provide an exceptionally rich data set that has revealed how Saturn's atmosphere evolved in the 5 years since the end of the Cassini mission. Section 2 describes the processing steps applied to MIRI/MRS data, including algorithms to address saturation and instrument artifacts. Section 3 provides an overview of the spatial structure and spectral features observable by MIRI/MRS, and compares the observations to Cassini data in 2017 to reveal seasonal variability. Section 4 then describes our spectral modeling approach, including both reflected sunlight and thermal emission, which is used in Section 5 to assess Saturn's northern-summer temperatures and zonal wind shears; the spatial distribution of aerosols, tropospheric condensables and disequilibrium species; and a broad range of stratospheric species to trace stratospheric chemistry and circulation.

2. JWST MIRI Data Processing

2.1. MIRI/MRS Observations

The MIRI/MRS instrument (Wells et al., 2015) consists of four IFUs (channels 1–4) spanning the 4.9–27.9 μm range with spectral resolutions from $R \sim 1,330$ at 27.9 to $R \sim 3,710$ at 4.9 μm (Labiano et al., 2021). Each IFU

has a different slice width (from 0.176 to 0.645″) and pixel size (from 0.196 to 0.273″), and thus field of view, such that they provide different spatial coverage and sampling on Saturn's disc in Figure 2. Although all four IFUs observe simultaneously (channels 1 and 2 on a SHORT detector, channels 3 and 4 on a LONG detector), a grating wheel with three different settings (A, B, C) is needed for full coverage, leading to a short delay between observations of adjacent portions of the spectra. The four IFUs and three grating positions provide 12 individual sub-bands, each with its own wavelength coverage and spectral resolution.

The Saturn system observations were part of the Solar System Guaranteed Time Observations awarded to H. Hammel, and collated as programme 1247. The MRS observations were the first science observations to be executed after a brief hiatus of operations (24 August 2022–12 November 2022), when the MRS grating wheel was found to be experiencing increased friction when moving between (A) short, (B) medium, and (C) long wavelength settings. The Saturn observations were redesigned to be executed in reverse-wavelength order (C, to B, to A), with no detriment to the science, and were executed shortly before Saturn left JWST's field of regard in 2022 (i.e., moving below the 85° elongation angle from the Sun, as Saturn opposition was earlier in the year on 14 August 2022).

MIRI/MRS provided a full latitude scan from Saturn's equator to the north pole using three separate mosaic tiles, with a final tile capturing the western ring ansa, as shown in Figure 1. Each tile covered the full 4.9–27.9 μm spectrum, with saturation encountered in the brightest hydrocarbon emission features. Saturn's angular diameter was 16.9″ at the time of the observations (9.8 AU from JWST, moving away from the observer at 29 km/s), and the spatial coverage of each tile varies with wavelength, from $3.2 \times 3.7″$ at the shortest wavelength (4.9 μm) to $6.6 \times 7.7″$ at the longest wavelength (27.9 μm).

The MIRI/MRS observations required five separate pointings on 13 November 2022 and 14 November 2022, as shown in Figure 2. The western ring ansa was observed first (03:00–04:06 UT), followed by an offset 90″ north of Saturn (04:11–04:27 UT) to determine instrumental artifacts in the MRS observations. JWST then pointed to Saturn's northern hemisphere, targeting 45°N (05:40–06:44 UT), 15°N (06:50–07:55 UT), but failed to re-acquire a guidestar to complete the final pointing toward Saturn's north pole. Given that Saturn was about to depart from JWST's field of regard, rapid instructions to re-execute the failed MRS footprint were uploaded to the observatory, enabling the final tile at 75°N on 14 November 2022 (21:58–23:05 UT), around 36 hr after the skipped observation was reported.

With the exception of the 15°N observation, all MRS tiles used five groups (i.e., individual 2.8-s frames) with the FASTR1 readout pattern, eight integrations, and a four-point extended-source dither pattern (no dithers were used for the offset "background" frame). The equatorial footprint used four groups and 10 integrations, to test the impact of using a smaller number of groups on ability to radiometrically calibrate MRS (no problems were identified).

2.2. MIRI/MRS Data Processing

The MIRI/MRS observations were reduced using the JWST pipeline version 1.9.4 and calibration reference files 1046, available under calibration reference context jwst_1046.pmap at https://jwst-crds.stsci.edu/context_table/jwst_1046.pmap. These were applied to the stage-0 UNCAL raw data cubes downloaded from MAST. The final output of the pipeline (stage-3), when run automatically for the archive, are spectral images cubes for each MRS channel with individual dithers combined then rotated and interpolated into a sky reference frame. However, the Saturn data needed a significant amount of post-processing before being usable, such that the pipeline was run locally, applying all three data reduction stages separately to each dither position and tile. Stage 1 generates "slope images" (count rates) from the raw UNCAL data; stage 2 applies wavelength calibration and absolute flux calibration for each exposure; and stage 3 produces spectral image cubes from the input calibrated slope images—all steps are described in the JWST data processing manual (https://jwst-docs.stsci.edu/jwst-science-calibration-pipeline-overview/stages-of-jwst-data-processing). The pipeline's ResidualFringeStep was used to minimize the effect of spectral fringing, although this remained a challenge at longer wavelengths in Channels 3 and 4 (Wright et al., 2023). The default pipeline rotates and interpolates the final cubes into a sky reference frame, but given the significant artifacts from slice to slice (discussed below), we retained the final stage-3 data in the coordinate system of the IFUs (cube_build.coord_system = "ifualign") to allow later correction of flat field effects. These corrections must be performed before any attempts to combine individual MRS dithers, otherwise artifacts are blended together in the final products. Finally, our pipeline included improved wavelength calibration solutions, known as FLT-5, now available as the "specwcs" files under calibration reference context
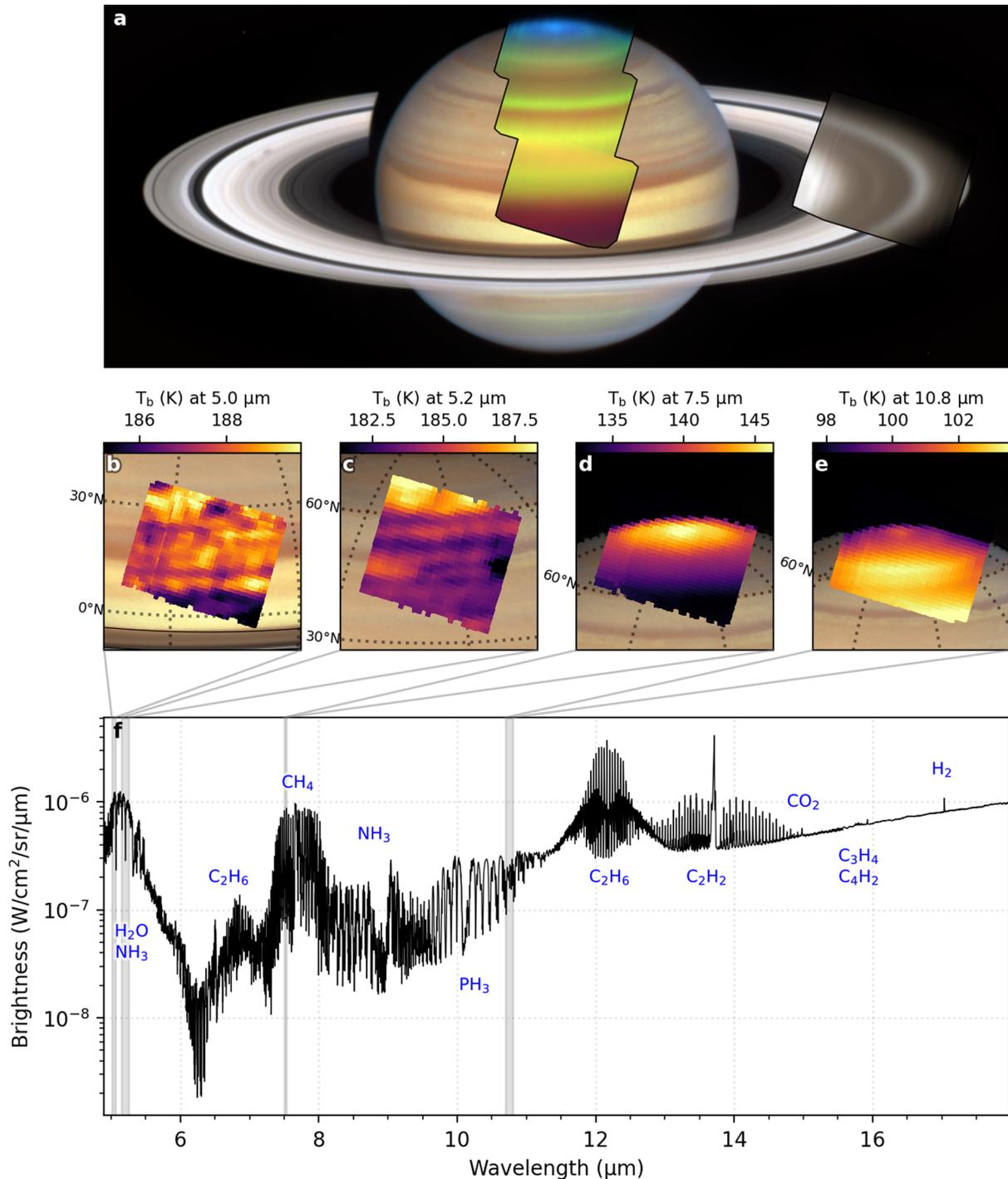
Figure 1. Montage of JWST Mid-Infrared Instrument/Medium Resolution Spectrometer observations of Saturn. Panel (a) shows RGB composites of the JWST observations (Saturn: $R = 10.3$ µm, $G = 10.1$ µm, $B = 11.6$ µm and rings: $R = 15.5$ µm, $G = 14.6$ µm, $B = 13.5$ µm) with an HST observation of Saturn in the background (Simon et al., 2023). Panels (b–e) show spatial structure on Saturn at a range of wavelengths as indicated by the gray shaded regions in panel (f). (f) Shows the average spectrum of Saturn with specific spectral features labeled.

jwst_1082.pmap (https://jwst-crds.stsci.edu/context_table/jwst_1082.pmap) (Argyriou et al., 2023), which were generated by fitting Jupiter and Saturn spectral models (this work) to the MRS data for each and every spaxel (the wavelength solution varied across the IFU), and estimating the required wavelength shift for each spaxel to align models and MRS data in the rest frame. These wavelength solutions were only possible below 15 µm where
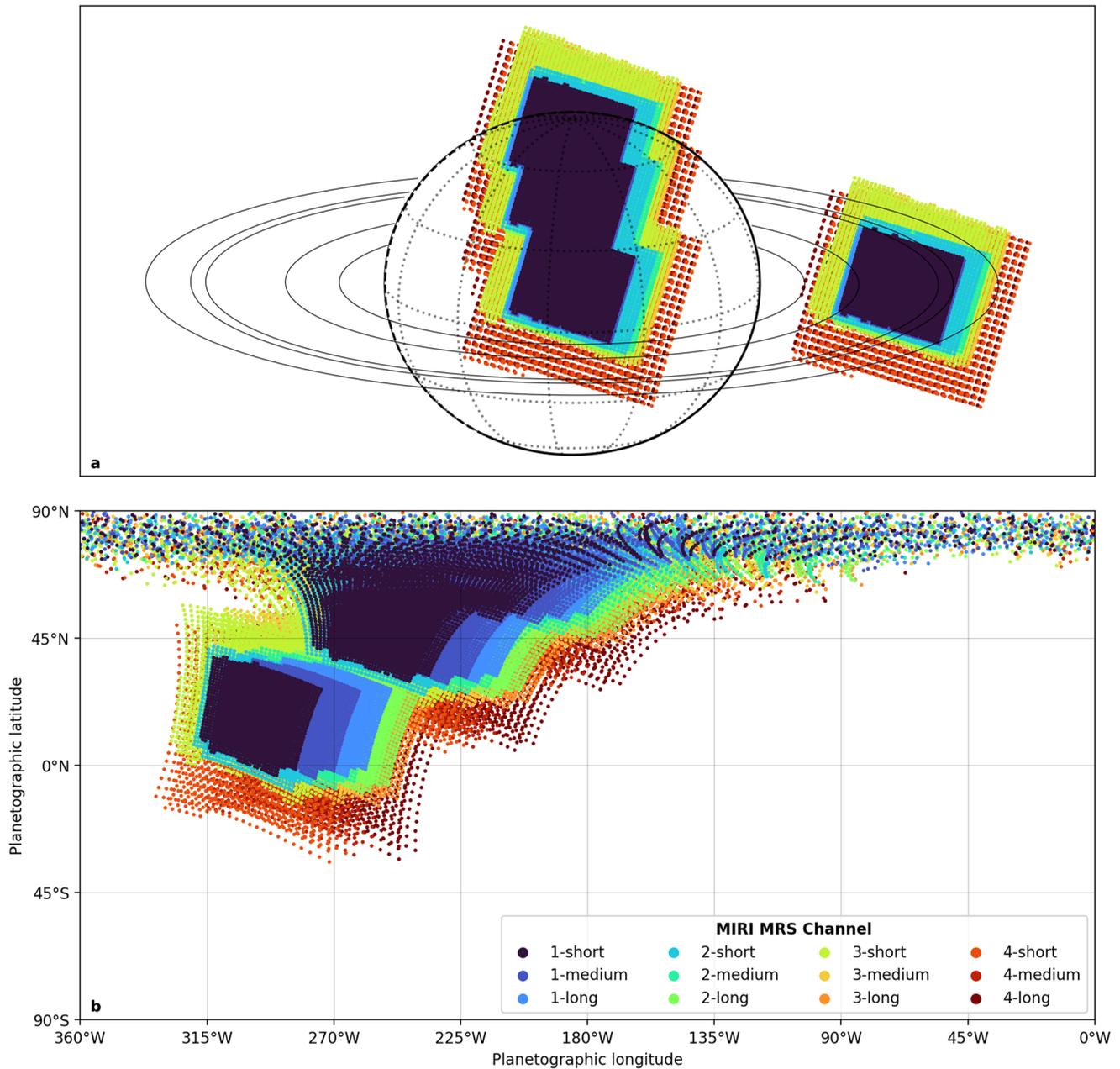
Figure 2. Spatial coverage of Mid-Infrared Instrument (MIRI) observations (a) relative to Saturn's disc and (b) mapped to Saturn's surface. Each dot represents the location of a single spaxel with the color indicating the MIRI channel. The background observation was located 90″ to the north of Saturn, so is not shown here (Saturn's disc has a diameter of ~17″).

strong and well-resolved spectral lines were evident, but enabled a significant improvement in spectral fits over the original pipeline.

As shown in Figure 3, significant flat field artifacts and saturation remained in the pipeline output cubes in the IFU-aligned frame. Therefore, we developed custom desaturation and flat field correction routines (discussed below) to correct these effects and produce our final science cubes.

2.3. Desaturation

In the brightest parts of Saturn's spectrum, the MRS detector becomes saturated, leading to a loss or corruption of data (e.g., Figure 3g). MIRI observations are split into a series of "groups," which each record the measured
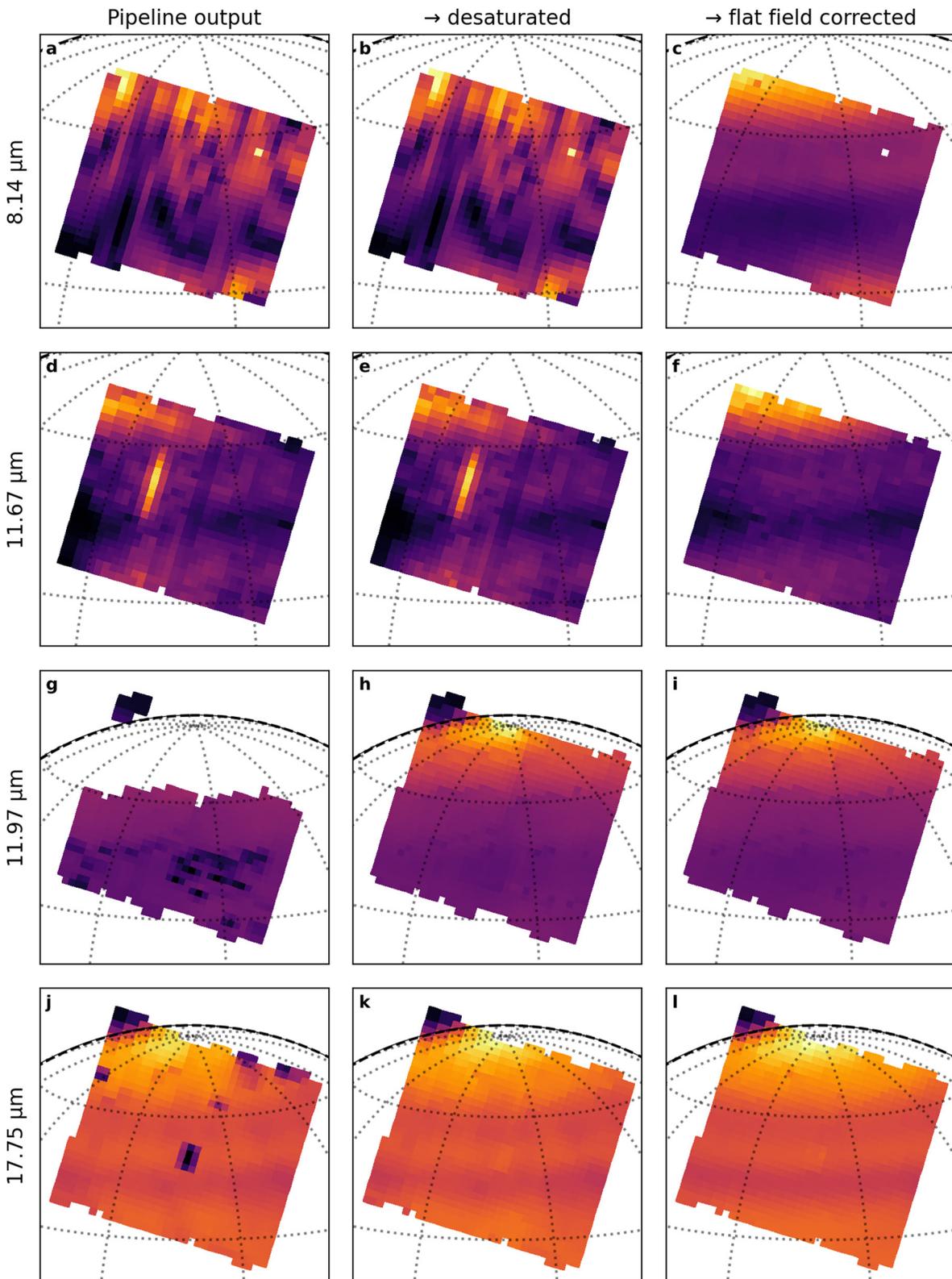
Figure 3. Example cube slices at different stages of our custom Mid-Infrared Instrument data reduction process. The first column shows the output of the standard JWST pipeline, which still contains significant flat field effects (a and d), saturation (g), and partial saturation (dark pixels in panels (g and j)). The second column shows the data after the desaturation step is applied and the third column shows the data after the flat field correction is applied.
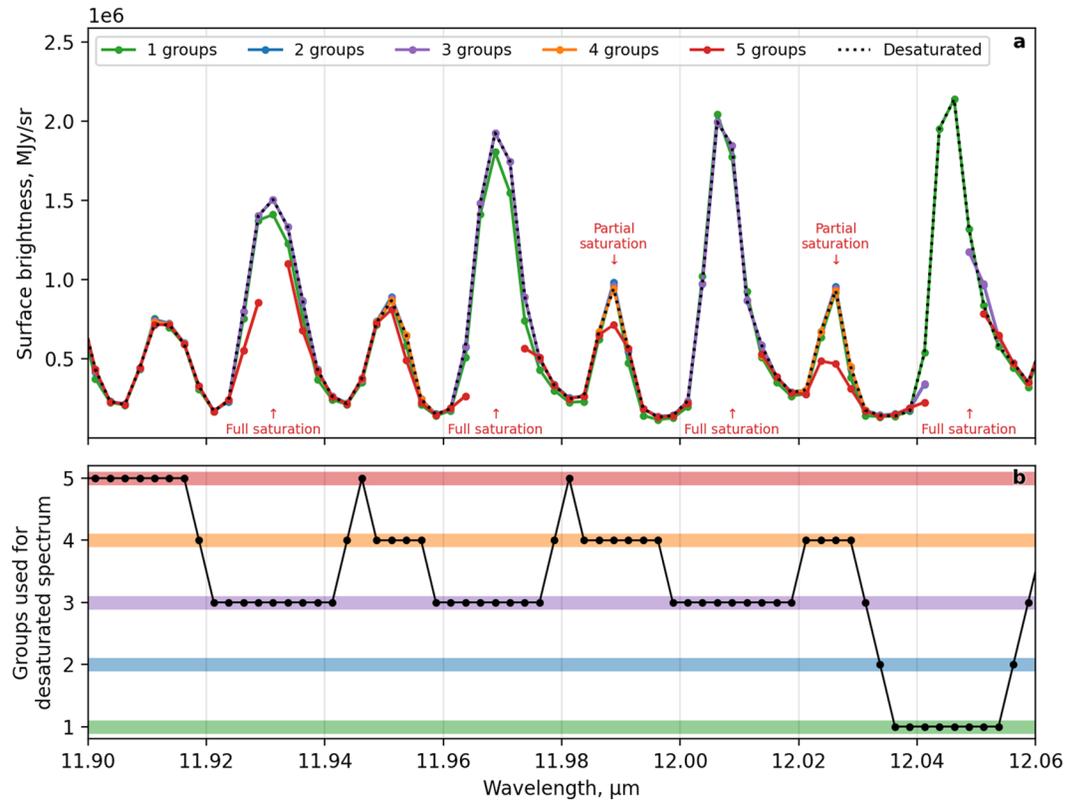
Figure 4. Example spectra showing the desaturation routine. (a) Shows the spectra using different numbers of groups, where the five group data (in red) is the "standard" pipeline output, which shows both saturation and partial saturation. The black dotted line in panel (a) shows the desaturated spectrum which is constructed using a varying number of groups, as shown in panel (b), to minimize saturation while maximizing SNR. The majority of the spectral range uses the full five group data, and only narrow regions (such as this one, in the ν_9 ethane emission band) require desaturation.

flux for a part of the whole exposure. The detector saturates when the integrated flux reaches a certain threshold, meaning that even if the full exposure is saturated, the first few groups in the exposure may still have useful data that was recorded before the detector saturated. Therefore, data reduced using different numbers of groups can be used to desaturate (i.e., "fill in") saturated parts of the spectrum.

Our data processing routine modifies the UNCAL raw data cubes to create versions containing the full range of groups (i.e., for the observations which have five groups in total: 1, 2, 3, 4, and 5 group versions are created). These different versions are all run through the standard JWST pipeline, creating five different versions of each science cube, each of which effectively has a different integration time. These five cubes are then merged into a single desaturated cube by dynamically selecting the highest number of groups possible to maximize SNR while minimizing saturation, as shown in Figure 4.

The desaturation routine operates by comparing the different versions of each spectrum (the colored lines in Figure 4a). The routine works iteratively, starting with the largest number of groups n, then replacing bad regions of the spectrum with the $n-1$ group spectrum. This is repeated until none of the spectrum contains "bad" data, or the 1-group spectrum is reached. The following regions of the spectrum are treated as bad data and replaced:

- Regions flagged as saturated by the JWST pipeline (marked as "full saturation" in Figure 4a).
- Regions that appear partially saturated, but have not been flagged as saturated by the JWST pipeline. Regions are classed as partially saturated where n group data is <90% of the brightness of the $n-1$ group data.
- Regions where the n group data is >120% of the brightness of the $n-1$ group data are also flagged as outliers, likely caused by cosmic ray hits.

The desaturation routine is skipped for regions of the spectrum with a SNR < 300, as these would not be expected to experience saturation, and high noise levels could lead to false positives when flagging bad regions of the spectrum.
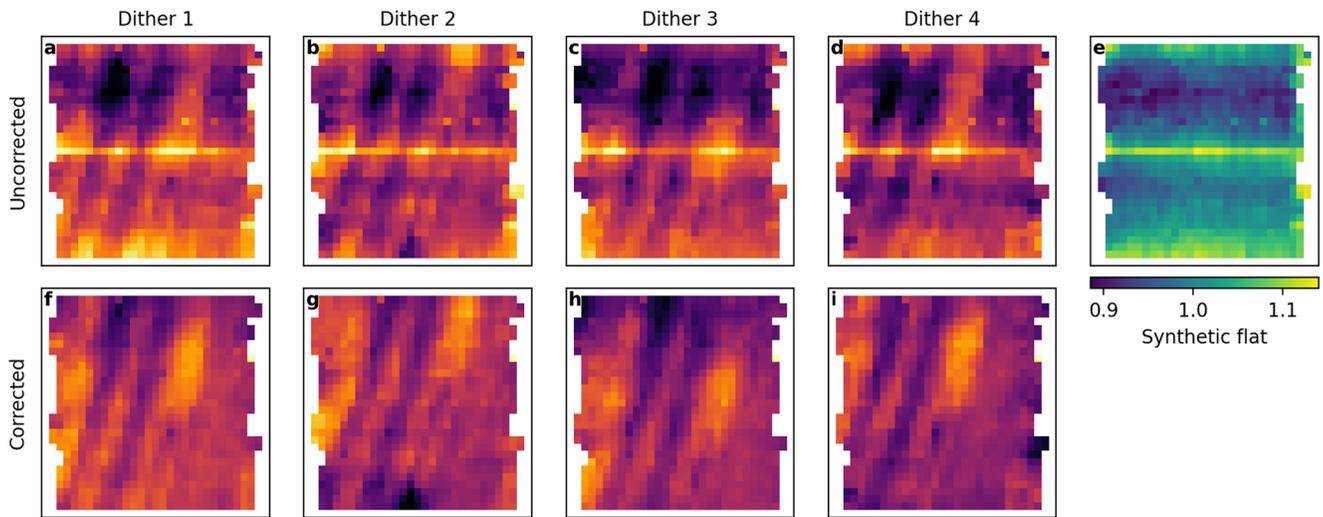
Figure 5. Example images at 5.07 μm (channel 1-SHORT) before (a–d) and after (f–i) the synthetic flat field (e) is applied. The images are shown in the integral field unit (IFU) frame, where north is to the top left. The flat field effects in panel (a–e) (such as the bright line across the center of each image) are fixed in the IFU frame, whereas the observed spatial structure on Saturn varies in position on the detector with the different dithers, allowing flat field structure and real spatial structure to be differentiated.

Initial testing of this routine found residual effects at the edge of spectral regions flagged as bad data, so any regions of the spectrum flagged as bad data are expanded by two spectral points. Additionally, the number of groups used for neighboring spectral points is only allowed to change by 1 (i.e., a spectrum cannot immediately jump from 1 group at one wavelength to 5 groups at the next wavelength). A similar filter is applied in image space, so at a specific wavelength, neighboring pixels can only vary by one group.

The parameters of the desaturation routine were selected by inspecting spectra (e.g., Figure 4) and images (e.g., Figure 3) at a wide range of wavelengths, including regions of the spectrum that do and do not experience saturation. Almost all the spectral range uses the full five groups (or four groups for the equatorial tile), with only the specific spectral and spatial regions (<10% of all spectral points) that experience saturation replaced with fewer groups.

2.4. Flat Field Correction

After desaturation, significant flat field effects remained visible in the cubes, particularly at shorter wavelengths (e.g., Figures 3b and 3e). These effects typically appeared as regular banding patterns aligned along the IFU slices, stripes, and swirls that varied with wavelength, and in many cases completely obscured any detail on Saturn. As shown in Figure 5, these patterns remained fixed in location on the detector for different dithers (and tiles), demonstrating that they are clearly an instrumental artifact.

These observed flat field patterns may be caused by small discrepancies between the reference flat field images used in the pipeline and the "true" flat field response of the detector. It is also possible that part of the observed apparent flat field is caused by residual artifacts remaining after the pipeline's stray light correction step. For simplicity, we refer to the entire observed pattern as the "flat field effect," regardless of its origin.

To correct for these flat field effects, we used the Saturn observations themselves to create a flat field for each channel and band. We assumed that the flat field can be treated as a purely multiplicative effect, with a corrected cube created by dividing the observed cube by the synthetic flat cube. Note that the background observation, 90″ north of Saturn, did not show the same artifacts, suggesting that the flat field is sensitive to how the target illuminates the detectors and IFU slices.

Our flat generation routine uses a set of four dithered observations to create a synthetic flat field image for each wavelength. We match pairs of pixels that observe (approximately) the same location on the surface of Saturn in different dithers, and assume that any variation in brightness between these pixels is caused by differences in the
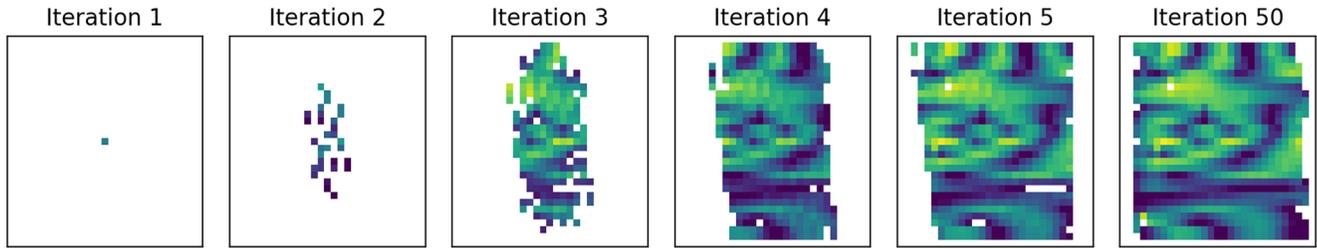
Figure 6. Example flat field at 8.14 μm after the first five iterations of the flat field generation routine, and after the final 50th iteration. The flat is seeded with an initial value for the first iteration, which then uses the corresponding pixel ratios (derived from the dithered observations) to propagate the flat values and fill the image. White pixels have a value of NaN, and the NaN values in the final flat field are regions of the detector that do not contain any data.

flat field for these pixels. The ratio of brightness values of all of the pairs of pixels can then be used to construct a flat field image at each wavelength:

1. The input data files for each dither are "navigated" to calculate the latitude/longitude coordinates and illumination angles for each pixel. This navigation uses the WCS metadata in the FITS headers (to convert from pixel to celestial coordinates), which is derived from JWST's pointing information. To validate the navigation, we compared the navigated and observed positions of Saturn's limb and rings, and found that no additional manual adjustments were needed.

2. The four dither input images are filtered to set extreme values (outlier pixels and pixels with emission angles >75°) to NaN to prevent any outliers contaminating the flat. Wavelengths where the average SNR < 10 are skipped as the constructed flat would be too contaminated with noise.

3. Corresponding pixels are identified by matching valid pixels that observe a similar location on Saturn in any of the four input dithers, using the navigated latitude/longitude coordinates for each pixel from step 1. An oval footprint is used around each pixel (in latitude/longitude space), and any pixels that fall within this footprint are treated as observing the same part of Saturn. The height (North-South direction) of the oval h is set at half of the average difference in latitude between neighboring pixels, and the width (East-West direction) of the oval is set as $w = 4h$. This elongated oval footprint is used as Saturn has much more variation in the North-South direction than the East-West direction, so it matches more similar pixels than a simple circular footprint would.

4. For each pair of corresponding pixels, A and B, we calculate the ratio of observed pixel fluxes $R_{AB} = O_A/O_B$. Assuming that the flat field is a multiplicative effect, we can treat each pixel's observed flux $O_i = S_i F_i$ as the "true" flux from Saturn S_i multiplied by the flat field for the given pixel F_i. As we define these corresponding pixels to observe (approximately) the same region of Saturn's surface, we assume that the original flux from Saturn is equal for both pixels, $S_A = S_B$, allowing the calculated ratio to be reduced to $R_{AB} = (S_A F_A)/(S_B F_B) = F_A/F_B$, giving the ratio of the flat field values for the two pixels.

5. The set of calculated pixel ratios are then used to construct the flat field image. A flat image is initialized with the central pixel value set to 1, and all other values set to NaN, and we then iteratively construct the flat using the calculated ratios to propagate values. At each iteration, every pixel value in the flat is updated to $F'_A = \text{median}(R_{Ai} F_i)$ where the F_i are all the non-NaN corresponding pixels. After all the updated values are calculated at each iteration, any pixels outside the range $2/3 < F_i < 3/2$ are set to NaN to protect against outliers. After removing outliers, the flat is then divided by the mean pixel value. The routine is run for 50 iterations to allow the constructed flat to converge on a consistent solution. Figure 6 shows an example flat field at different generation steps.

6. This constructed flat image is slightly under-constrained, as all the pixels can be multiplied by an arbitrary scaling factor and still provide a self-consistent result. Therefore, we scale each flat image so that the mean value of the pixels is unity, that is, $\frac{1}{N}\sum_i^N F_i = 1$. This ensures that the application of the flat does not change a spectrum calculated by averaging all the pixels in an entire cube.

Synthetic flat cubes were generated from the four dithers associated with the 15°N and 45°N tiles, and then averaged to produce the final flat cubes used to correct the data (the 75°N tile and ring observation included too much background sky to be useful). The algorithm parameters were refined by studying the flats generated from the different tiles and the quality of the flat corrected data.

Special care was taken to ensure the flats did not contain any features of Saturn's atmosphere, and to ensure that the flats from different tiles produced consistent results. Comparisons of sets of dithered images (e.g., Figure 5)

allows structure from the flat field (fixed in detector location, identical between tiles) and real structure on Saturn (variable in detector location, different in each tile) to be differentiated. Regions of the spectrum with and without significant spatial structure were studied in detail, as well as the entire spectral range using animations that compared sets of dithers at each wavelength (see Supporting Information S1). The 75°N and rings tiles also provided useful checks, as these tiles were well corrected, even though they were not used in generating the synthetic flats.

As shown in Figure 5, the synthetic flats are able to correct both small-scale (1–2 pixel) and large scale (>10 pixel) variations in the sensitivity of the detector, including in regions with significant spatial structure on Saturn. The application of the flats helped to reveal spatial structure in the Saturn observations that was often completely obscured by the sensitivity variations, and prevented any spurious spatial variation being treated as real spatial variation on Saturn's surface.

2.5. Zonal Averages

Zonal averages were calculated from the observed data using the following routine:

1. All observed pixels, from all tiles and dithers, are binned into 1° latitude bins.
2. Within each bin, the median spectrum is calculated from all spectra in the bin. The 1/3 of the spectra with the largest RMS relative to this median spectrum are then discarded. This ensures the final zonal averages are protected from the effect of outlier pixels. Median averaging is used here (rather than mean) to ensure any extreme outlier pixels do not cause "good" spectra to be discarded.
3. The mean spectrum for each bin is calculated from the remaining 2/3 "good" spectra. This mean spectrum is used as the zonal average for each latitude bin, which is then used for spectral modeling in subsequent sections.

3. Data Set Overview

3.1. Saturn's Spectrum

An average of MIRI/MRS observations of Saturn's atmosphere is shown at the bottom of Figure 1 for 4.9–18.0 μm, omitting MRS data from the longest channel (17.7–27.9 μm) due to ongoing challenges with fringe removal and calibration. Below ~7.3 μm, the spectrum is shaped by a combination of scattered reflected light from aerosols (notably within the deepest absorption bands and near 6 μm) and thermal emission. The 5-μm window is sculpted by PH_3 lines below 5.2 μm (ν_1 at 4.3 μm) and NH_3 above 5.2 μm ($2\nu_2$ at 5.32 μm, ν_4 at 6.15 μm), along with narrow absorption bands of H_2O (5.1–5.4 μm) and AsH_3 (4.9–5.0 μm). Bright emission from the 5-μm window implies low aerosol opacity, so cloud bands and small discrete features appear in silhouette in Figures 1b and 1c against the bright background glow from Saturn's 4–6 bar region. Bright reflection near 6 μm provides a means of constraining upper tropospheric aerosols. Hydrocarbon emission from CH_4 (ν_2 at 6.5 μm) and C_2H_6 (ν_8 at 6.8 μm; ν_6 at 7.3 μm) also contribute to this 4.9–7.3 μm range. This range is particularly noteworthy as it has only been previously observed by ISO/SWS in the disc-average (Encrenaz, 2003), and neither Cassini/VIMS ($R \sim 300$ at 5 μm) nor Cassini/CIRS ($R \sim 2,800$ at 7.0 μm) could observe in the 5.1–6.9 μm range. Thus MIRI channel-1 provides access to tropospheric NH_3 and H_2O, along with the properties of Saturnian aerosols, in this range for the first time, with spectral resolutions of $R \sim 3,100$–3,750.

Aerosol contributions diminish at longer wavelengths in channels 2 and 3 (7.3–18.0 μm), which are dominated by the collision-induced absorption due to H_2 and He, with emission and absorption features superimposed. PH_3 (ν_2 at 10.08 μm, ν_4 at 8.94 μm) and NH_3 (ν_2 at 10.5 μm) provide absorption features that dominate the 8–12 μm range; with strong emission features from methane (CH_4 ν_4 at 7.7 μm), acetylene (C_2H_2 ν_5 at 13.7 μm) and ethane (C_2H_6 ν_9 at 12.2 μm); and weaker emission features from CO_2 (ν_2 at 14.9 μm), diacetylene (C_4H_2 ν_8 at 15.9 μm), methylacetylene (C_3H_4 ν_9 at 15.8 μm), ethylene (C_2H_4 ν_7 at 10.5 μm), propane (C_3H_8 ν_{26} at 13.4 μm) and benzene (C_6H_6 ν_4 at 14.83 μm). The H_2 S(1) quadrupole at 17.03 μm and its associated dimer absorption can be seen in Channel 3-Long, but the S(0) quadrupole at 28.2 μm is just outside the MRS range.

The spectral database used in MRS modeling was initially based on that used for Cassini retrievals (Fletcher et al., 2018b), with updates to AsH_3 (Coles et al., 2019) and CH_4 (Adam et al., 2019) from the ExoMol database (Tennyson et al., 2016), and GeH_4 from HITRAN (Gordon et al., 2022). Voigt broadening was used for all bands– the sub-Lorentzian lineshape of Bailly et al. (2004) did not have an impact on the quality of the spectral fits. The
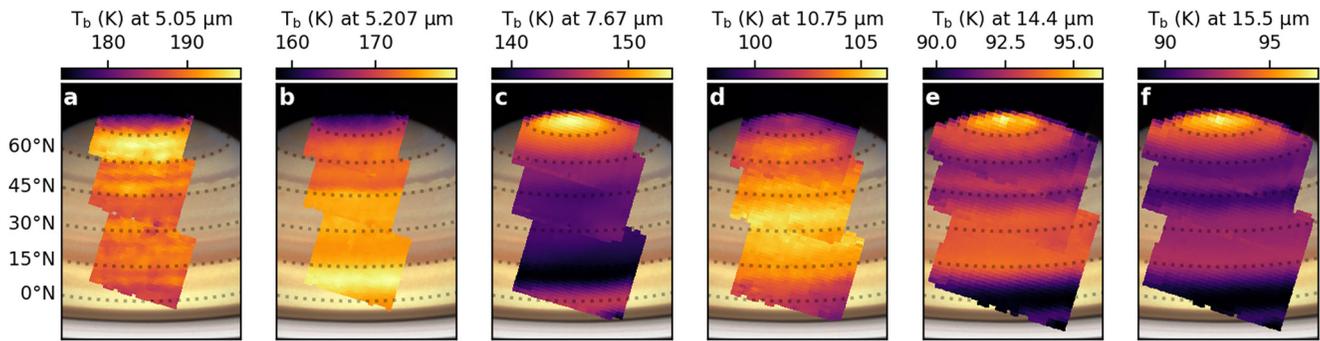
Figure 7. Composite images created by combining all three Saturn tiles to show the equator-to-pole variation in brightness temperature at different wavelengths. 5.05 μm senses aerosol opacity in the deep troposphere (3–6 bars), whereas 5.207 μm is in a strong NH_3 absorption and senses a blend of thermal emission and reflected sunlight from upper tropospheric aerosols. 7.67 μm senses stratospheric temperatures (0.1–5 mbar) via CH_4 emission; whereas 10.75 μm senses a blend of tropospheric temperature and ammonia opacity near 400–600 mbars. 14.4 and 15.5 μm are primarily sensitive to the H_2-He continuum, sounding tropospheric temperatures in the 100–300-mbar range. Note that each tile observed a different longitude range, but are shown overlapping here for simplicity—this causes some artificial inconsistencies in brightness at regions of overlap.

line database was used to calculate k-distributions for each gas within each of the 12 MRS subbands, using the wavelength grid from stage 3 of the standard pipeline, and the wavelength-dependent resolving power of each channel determined from ground-based measurements (Labiano et al., 2021). Note that in-flight commissioning updates to the spectral resolution (Jones et al., 2023) have not been incorporated into our spectral models at this stage.

Collision-induced absorption of H_2 and He was included based on their dimer absorptions (Fletcher et al., 2018a). During the course of the spectral fitting, residuals between model and data were used to identify missing bands of known species, and to search for any new species. Multiple bands of propane are observed on Saturn for the first time—only ν_{26} at 13.4 μm had been included in our line database based in GEISA (Delahaye et al., 2021), and had been previously used to study the propane distribution (Fletcher et al., 2018b; Guerlet et al., 2009). Residuals at high latitudes revealed the presence of the ν_7, ν_{20}, ν_{21}, and ν_8 emission bands at 8.63, 9.49, 10.85, and 11.51 μm, respectively, for the first time. These were introduced into our line database using the pseudo-linelist of Sung et al. (2013), and the improvement in spectral residuals are shown in Figure S6 in Supporting Information S1.

The GeH_4 ν_2 band at 10.74 μm is too weak to be seen, lost amongst numerous NH_3 absorption features. The AsH_3 ν_4 band at 9.97 μm does have a detectable signature on the edge of a PH_3 absorption line, but in a region of the spectrum that is affected by MRS fringing at the longward end of channel 2-medium. The small spectral feature is reproduced by an abundance of ~0.4 ppb, with a decline from equator to pole that cannot be explained by fringing. Nevertheless, precise constraints must await more robust defringing strategies. Finally, we see no evidence of emission from the HCN ν_2 at 14.05 μm, discussed in Section 5.4.

3.2. Spatial Structure

Figure 7 shows selected wavelengths from the three MIRI/MRS 4.9–27.9 μm cubes spanning from Saturn's equator to the north pole. Given Saturn's relative longitudinal homogeneity, these can be taken as a good approximation to a zonal mean, which is calculated as described in Section 2. Figure 8 then shows the difference between the zonally averaged brightness and the mean brightness temperature spectrum, highlighting strong gradients as a function of latitude. These gradients are compared to the cloud-tracked zonal winds from Cassini in both the continuum and methane bands (Figure 8c, García-Melendo et al., 2011), showing how thermal-infrared brightness is related to the peaks of the eastward and westward jets. We also compare the MIRI/MRS maps (acquired in November 2022) to visible-light reflectivity scans acquired by Hubble (HST) in September 2022 (Figure 8b, Simon et al., 2023), to show how brightness temperature and aerosol reflectivity are related. The zonally averaged reflectivity in 10 HST WFC3/UVIS filters has been normalized for plotting purposes, to highlight the similarities in the location of strong brightness gradients.

Together, the composite images of Figure 7 and the zonal-mean brightness in Figure 8 reveals a wealth of detail. The exquisite sensitivity of MRS, even compared to previous spectroscopic maps from Cassini, reveal Saturn's
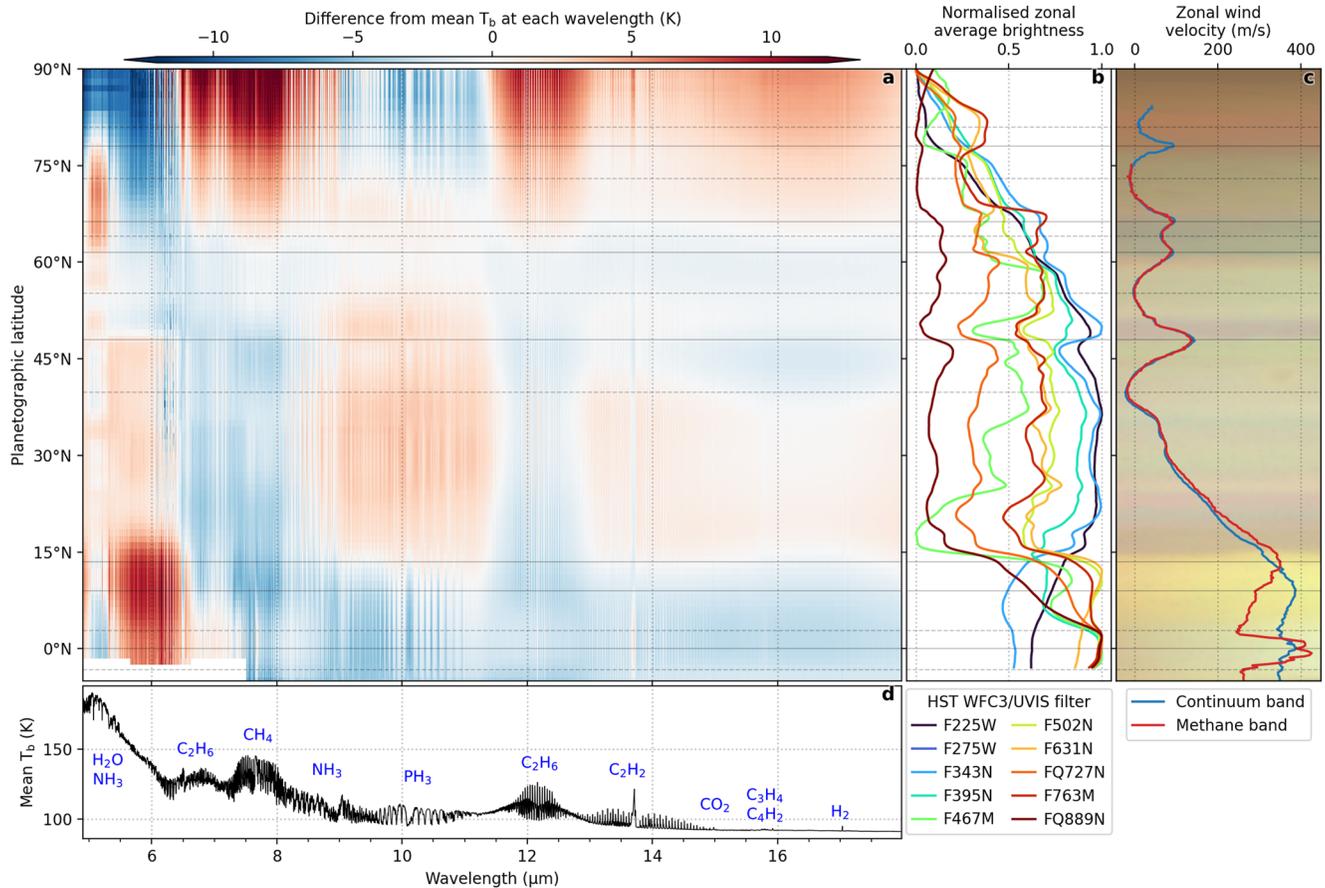
Figure 8. Variation in Saturn's zonal average brightness temperature with wavelength and latitude. (a) Shows the difference from the mean brightness temperature spectrum (d), where red areas are brighter than the average and blue areas are dimmer. (b) Shows the normalized zonal average brightness of HST observations of Saturn in September 2022 (Simon et al., 2023) and (c) shows Saturn's zonal wind profiles (García-Melendo et al., 2011). Solid and dashed horizontal lines in panels (a–c) indicate the peaks and troughs of the zonal wind profiles, respectively. The background of panel (c) shows part of the color composite map of Saturn created from the HST observations.

banded structure in both reflected sunlight and thermal emission. The following three features stand out in the meridional (latitudinal) direction:

- *Belt/Zone Structure*: The strongest meridional gradients in tropospheric and stratospheric brightness temperatures are co-located with the peaks of the eastward and westward jets, as measured at Saturn's cloud tops (García-Melendo et al., 2011), supporting a geostrophic balance between the winds and temperature gradients via the thermal windshear equation, and the decay of Saturn's tropospheric winds with altitude (Conrath & Pirraglia, 1983; Pirraglia et al., 1981). At mid-latitudes where Ferrel-like meridional circulation cells are expected to dominate (Fletcher et al., 2020a), Saturn's zones are defined as cool, anticyclonic bands equatorward of eastward jets, whereas the belts are warm, cyclonic bands poleward of eastward jets (Del Genio et al., 2009). MIRI continuum emission from the troposphere (e.g., Figures 7e and 7f) reveals subtle cool zones equatorward of eastward jets at 31.5° (an inflection in the broad equatorial jet), 47.8°, 61.5°, and 78.0°N, in addition to the broad cool Equatorial Zone at <9.2°N where continuum-band cloud tracking reveals a maximum eastward windspeed (García-Melendo et al., 2011). Stratospheric banding is more subtle, but a bright equatorial band is observed in methane emission at 7.67 μm and in the peak of the acetylene emission at 13.7 μm (corresponding to the equatorial stratospheric oscillation, Orton et al., 2008; Blake et al., 2022).

- *NPSV*: The warm NPSV, defined by the strong gradient in stratospheric brightness temperature near 78°N, is visible throughout the MIRI/MRS data set, particularly near 7–8 μm sensing stratospheric CH_4, and in regions of tropospheric continuum emission longward of 14 μm. This should be contrasted with generally low polar brightness temperatures in the 5–6.5 and 9–11 μm regions that probe higher pressures. The NPSV formed during northern spring (Fletcher et al., 2018b) and is expected to have reached its maximum contrast with
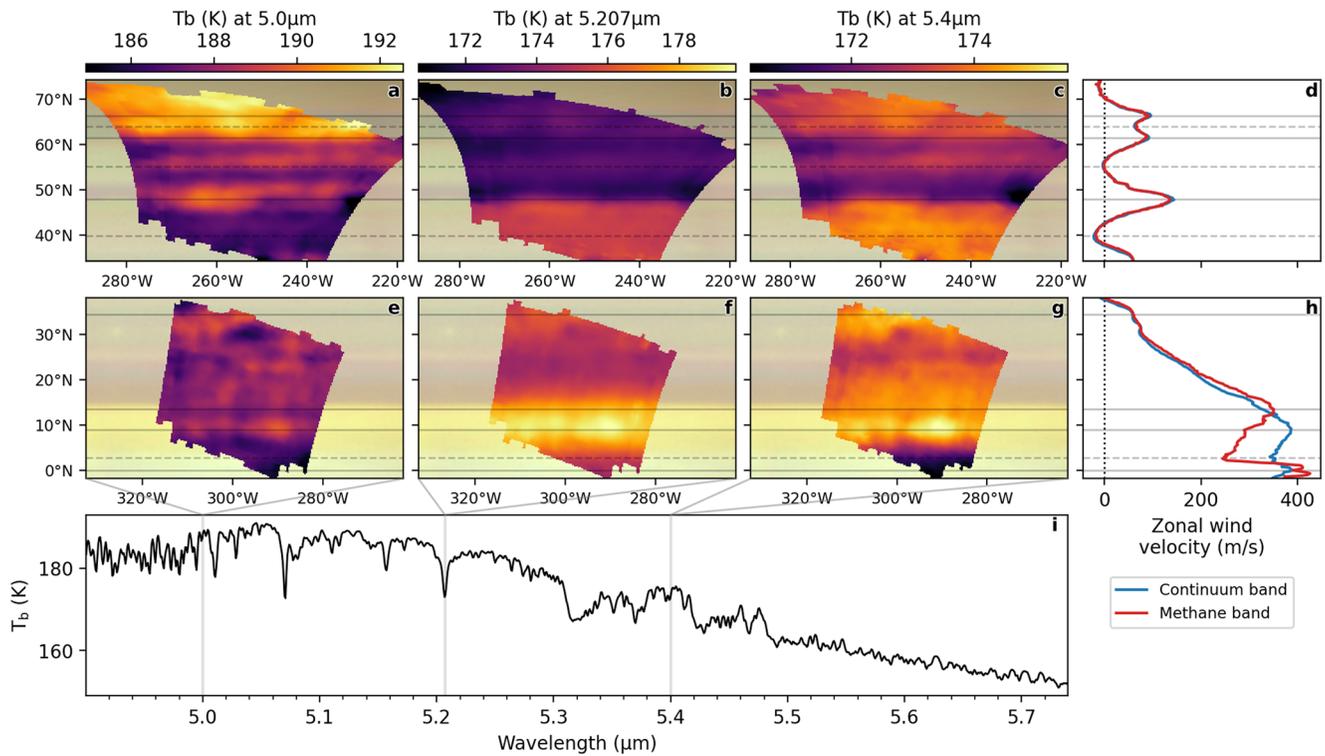
Figure 9. Mapped spatial structure in channel 1-short for low- and mid-latitudes. (d, h) Show the zonal wind velocities (García-Melendo et al., 2011) and (i) shows an example brightness temperature spectrum. While all panels sense a blend of thermal emission and reflected sunlight, panels (a, e) primarily reveal deep thermal emission modulated by overlying aerosol opacity, whereas panels (b, c) and (f, g) primarily reveal reflectivity variations from aerosols in the upper troposphere. Solid and dashed horizontal lines indicate the peaks and troughs of the zonal wind profiles, respectively. The backgrounds of (a–c and e–g) show the color composite map of Saturn created from the HST observations.

respect to lower latitudes in 2021–2022 (confirmed by ground-based thermal imaging Blake et al., 2022), and to decline in visibility in the coming years—see below for discussion of seasonal evolution since the end of the Cassini mission in 2017. Embedded within the NPSV, the central North Polar Cyclone (NPC) discovered by Cassini (Fletcher et al., 2008) remains visible in the MIRI/MRS maps as a peak in brightness temperature right at the pole (Figures 7c–7f).

- *Deep Cloud Structure*: As has been previously shown by ground-based imaging at 5.1–5.2 μm (Yanamandra-Fisher et al., 2001) and Cassini/VIMS spectroscopy (<5.1 μm, Baines et al., 2006; Fletcher et al., 2011), MIRI 5-μm maps in Figure 7a and the zonal mean in Figure 8 reveal cloud banding on a much finer spatial scale than the broad belts and zones defined by the temperature field. Indeed, the distribution of aerosols revealed by MIRI spectroscopy between 4.9 and 7.3 μm is a good match for the albedo contrasts in Figure 8c, but are not a good proxy for Saturn's belts and zones (Fletcher et al., 2020a)—aerosols do not simply condense where it is cold, and sublimate where it is warm, with a more complicated pattern emerging. Rather, the finescale cloud banding observed at 5 μm is a closer match to that seen in visible light (e.g., Vasavada & Showman, 2005). Deep NH_3 absorption features in the 5.1–5.3 μm range, and in the 6-μm region, also reveal the contribution of reflected sunlight from upper tropospheric aerosols (Figure 7b)—without this reflection, there would be almost no radiance from these deep bands. The equatorial region is particularly bright in the 5.5–6.5 μm range in Figure 8a due to the presence of upper tropospheric aerosols observed in visible light in Figure 8a.

The deep clouds revealed by MIRI/MRS are shown in more detail in Figure 9, which uses only the shortest MRS channel (1A). Animations available in our supporting data set (Fletcher, 2023) show that Saturn's appearance changes dramatically with wavelength, from inside a deep absorption band (sensing sunlight reflected from upper tropospheric aerosols) to the intervening "continuum" (sensing deeper cloud opacity). The Equatorial Zone (0–9.2°N) is generally dark (e.g., high aerosol opacity), with a brighter band near 10°N marking the boundary with the NEB. At 5.0 μm small low-contrast features are observed up to the prograde jet at 48°N, but these cannot

be seen at 5.2 μm where reflected sunlight creates a more homogeneous appearance. Poleward of the 48°N jet, the 5-μm thermal emission increases substantially at the same time as the reflectivity sharply declines. We no longer see the 5-μm-bright, aerosol-depleted band near 35°–40°N that had dominated the appearance of the northern hemisphere after the 2010–2011 storm (Sromovsky et al., 2016), consistent with a re-population of the band by Saturn's seasonal aerosols in the decade since the storm, so that this band no longer stands out. This fading of the 5-μm storm emission is consistent with the ground-based record (Bjoraker et al., 2020). Fine banding is observed up to 61.5°N, when the 5-μm emission again rises substantially as 5.2 μm reflection falls, with bright emission continuing to the latitude of the hexagon at 78.0°N. Interior to the hexagon, the polar domain in Figures 7a and 7b is 5-μm dark, and also dark in reflected sunlight at 5.2 μm, consistent with its appearance in Cassini/VIMS observations in 2016 (Sromovsky et al., 2021).

Seasonally generated aerosols are not homogeneous over the whole of Saturn's northern hemisphere, but are confined by the banded structure—the reflected sunlight component in Figure 9b and the 5–6 μm range in Figure 8a decreases in distinct steps from the equator to the pole, with notable boundaries between the EZ and NEB (9.2°N) and at 48.7°N; the thermal 5-μm emission component shows a notable increase between 61.5° and 78°N, consistent with the lowest aerosol opacity there, and with the suggestion of cloud-clearing near 65°N in 2019–2020 (Bjoraker et al., 2020). A four-fold increase in aerosol opacity of upper-tropospheric hazes interior to the hexagon between 2013 and 2016 was observed by Cassini (Sromovsky et al., 2021), possibly accounting for the dark hexagon appearance to JWST in 2022. MIRI does not observe the hexagon latitude as a bright 5-μm band, which had been evident in VIMS observations in 2013 and 2016, suggesting continued increases in aerosol opacity in the polar domain, spreading to lower latitudes, but not yet reaching the 60°–78°N range.

Right at the equator, equatorward of 5°N, both the 5-μm brightness and the reflected sunlight drop to create an unusually dark band. This can be seen in Figure 8, where the dark band corresponds to subtle color contrasts in Hubble images from September 2022, and to a peak of reflectivity in several of the individual HST filters, notably the strong CH_4 band at 889 nm. Such a dark band was not evident in VIMS maps in 2006–2011, although this region was generally bland and diffuse at 5 μm, with several dark plume-like discrete features bordering it at 6°–7°N (Fletcher et al., 2011). This dark band coincides with the rapid increase in the upper tropospheric winds observed in the 890-nm CH_4 band i Figure 8c (García-Melendo et al., 2011). We will return to this unique region, and the challenging spectral fits, in Section 5.

3.2.1. Discrete Vortices and Hexagon

Although Saturn remains longitudinally homogeneous at most latitudes, we subtracted zonal averages from the MRS images to search for evidence for discrete features. Such longitudinal contrasts were only definitively observed in the shortest MRS channels in Figure 9, where significant structure is observed. In particular, we see a bright cloud-free region near 48°N, 261°W; at least two dark anticyclonic vortices near 48°N, 230°W and 30°N, 299°W; a patch of high 5-μm brightness at the edge of the equatorial zone near 10°N, 292°W; and spatial structure in the bright band surrounding the dark polar domain near 62°N, 215°W. In an effort to determine the history and longevity of these features, we compared the MIRI maps (13–14 November 2022) to HST observations (21 September 2022, Simon et al., 2023) and observations by amateur astronomers (using the PVOL database throughout November 2022, Hueso et al., 2018) to search for the presence of these discrete features in multiple data sets. Comparisons of the JWST and HST data are shown in Supporting Information S1.

Unfortunately, there were no conclusive detections of any of the features observed by MIRI in these supporting visible-light data sets. Given the ~7-week time gap between HST and JWST observations this is perhaps unsurprising, despite attempts to account for zonal drifts during this interval in Supporting Information S1. In particular, HST observations in September revealed the continued presence of the anticyclonic vortex (AV) that was generated by the 2010–2011 storm (Sayanagi et al., 2013) near 42°N, 190°W, and the presence of a pair of vortices near 63°N, 335°W that could be related to the coupled vortex system on the "double jet" near 62°–67°N studied by del Río-Gaztelurrutia et al. (2018). Whilst the shared latitudes are compelling, the limited longitudinal coverage of the MRS maps, combined with the 7-week time gap since Hubble, makes it unlikely that these are the same features. Indeed, the long-lived AV at 42°N was expected to be near 176°W on 13 Novmber 2022, and was therefore missed by MIRI (Figure 2). This strongly argues for contemporaneous MIRI/MRS spectroscopy and NIRCAM (or HST) imaging in future observing programs.

Finally, when the MIRI observations had originally been designed (assuming a 2018 launch), we had hoped to detect the vertices of Saturn's polar hexagon during northern summer, both in tropospheric and stratospheric

thermal emission (Fletcher et al., 2018b). Unfortunately, the decreasing sub-observer latitude in 2022 reduced the chances of success, and no convincing evidence of hexagon vertices can be observed, despite considerable work to clean up and combine the individual channel-1 dithers. We will likely need to wait to the 2040s for our next infrared views of the hexagon itself.

3.3. Seasonal Change Since Cassini

Before modeling the MRS spectra, we compare the calibrated JWST data to other observations in the mid-infrared. Although ground-based studies have been able to monitor morphological changes to Saturn's mid-IR emission since 2017 (Blake et al., 2022), these have typically been calibrated to match a low-latitude average of Cassini/CIRS radiances due to the difficulties arising from variable telluric contamination, making genuine assessments of global-scale temperature changes rather challenging. Figure 10 compares the MIRI 7–17 μm brightness with those from Cassini/CIRS in 2017. Three CIRS northern hemisphere maps (19 January 2017, 17 April 2017, and 26 August 2017), acquired from a near-equatorial sub-spacecraft latitude at a spectral resolution of 15 cm^{-1}, were combined and zonally averaged onto a 1° latitude grid. The MIRI/MRS zonal averages were convolved with the CIRS instrument lineshape to achieve the same low spectral resolution, and the differences are shown in Figure 10. Note that the viewing geometry for each latitude was approximately the same in 2022 and 2017, such that limb darkening/brightening should be negligible.

The 7–8 μm CH_4 emission in Figure 10c shows the change in Saturn's equatorial stratospheric oscillation (Fouchet et al., 2008; Orton et al., 2008), which reveals a brighter equatorial band in 2022 compared to 2017. This warm band is also visible at 7.65 μm in Figure 7. This is consistent with the ground-based record (Blake et al., 2022) which showed continued warming at the equator since the end of the Cassini mission. It is not, however, consistent with expectations from one Saturnian year earlier, where the equatorial band was in its cool phase in 1993–1995 during the same season. Thus the semi-annual nature of Saturn's equatorial oscillation remains in doubt (Blake et al., 2022; Sinclair et al., 2013).

The stratosphere from 10° to 35°N appears to be cooler in 2022 than in 2017, consistent with the idea of upwelling and adiabatic cooling in the summer hemisphere as part of an interhemispheric circulation from summer to winter, reminiscent of the Earth's Brewer-Dobson circulation (Bardet et al., 2022; Friedson & Moses, 2012). During northern winter (L_s = 310°), enhancements of stratospheric hydrocarbons detected by Cassini near 25°N (Guerlet et al., 2010) were consistent with stratospheric subsidence as part of a meridional circulation from summer to winter (Friedson & Moses, 2012). The cooler brightness temperatures measured by MIRI suggest that this circulation has now reversed by L_s = 150°, having switched direction near equinox in 2009 (Bardet et al., 2022). In the following sections, we will attempt to verify this via measurements of trace hydrocarbon species to determine vertical motions in the northern low-latitude stratosphere.

Poleward of 60°N, the MIRI/MRS observations reveal warmer temperatures than the Cassini/CIRS observations, consistent with the continued warming of the NPSV in Figure 7 as northern summer progressed. This is also true in the northern troposphere, sampled by H_2-He emission longward of 14 μm, which has warmed since 2017. Radiative models (Guerlet et al., 2014), combined with the viewing geometry from Earth (Blake et al., 2022), predict the visibility of the NPSV will drop considerably in the next 1–2 years as autumn approaches. Cooler MIRI north-polar temperatures at ∼10, 12.2, and 13.7 μm could be a consequence of differences in spatial and spectral resolution (particularly the spectral convolution in the Q-branches of ethane and acetylene), rather than reflecting a real change between 2017 and 2022.

As a further assessment of seasonal change, we compare zonal-mean scans of ground-based VLT/VISIR observations of Saturn at 7.9, 12.3, and 17.6 μm from 2016 to 2022 (Blake et al., 2022) to the results from CIRS and MIRI (see Figure S8 in Supporting Information S1). All three techniques capture the contrasts associated with Saturn's bands, with the 17.6-μm observations confirming the tropospheric warming during northern summer; and 12.3 μm showing the warm equatorial band and increased brightness of the NPSV. However, at 7.9 μm, Figure S8c in Supporting Information S1 shows the problems associated with scaling ground-based images to a low-latitude CIRS average, as it missed the stratospheric cooling between 10° and 50°N, and therefore over-estimated the brightness of the NPSV. So whilst the NPSV has warmed since 2017 (by 3–4 K in brightness temperature at 7.9 μm), the magnitude is smaller than that presented in ground-based studies (Blake et al., 2022). In summary, MIRI/MRS observations in 2022 reveal changes to Saturn's equatorial oscillation, unexpected
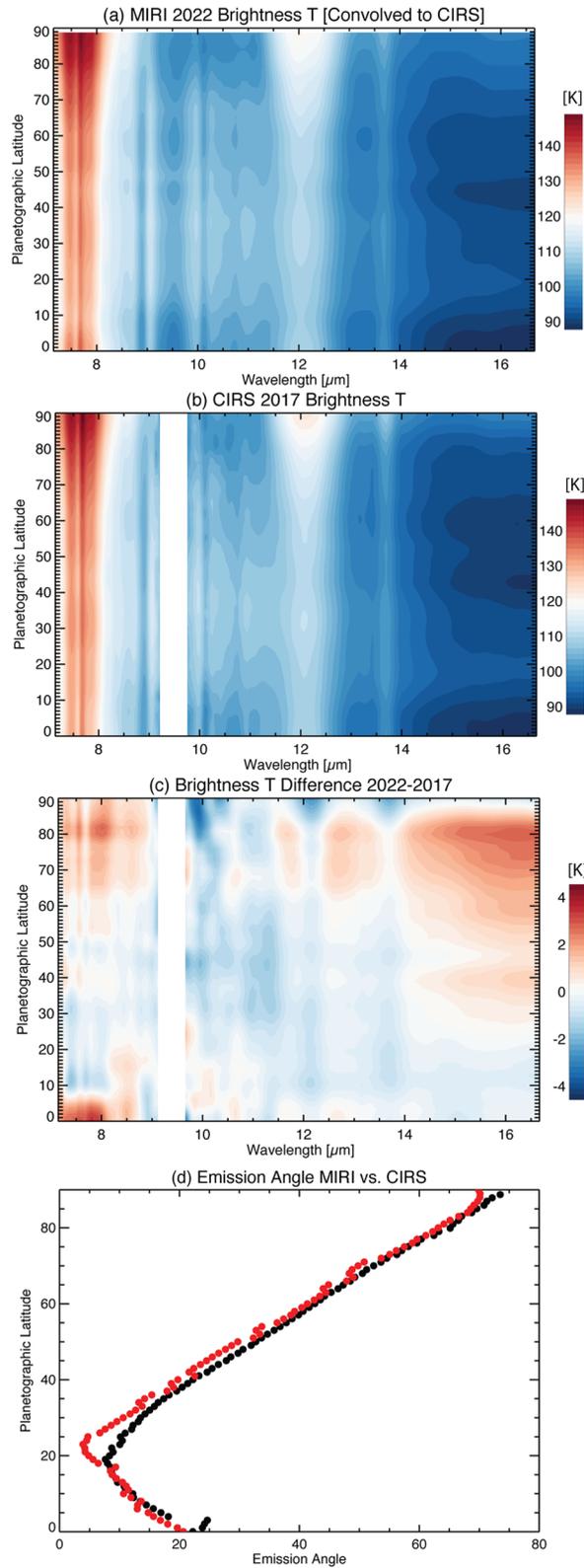
Figure 10.

stratospheric cooling equatorward of 40°N, tropospheric warming at most latitudes, and the continued warming of the NPSV.

4. Spectral Modeling

Although inspection of the cleaned MIRI/MRS cubes can demonstrate the spatial contrasts in Saturn's mid-IR emission associated with cloud banding and discrete storms, further progress can be made by inverting the MIRI spectra to determine Saturn's temperatures, zonal winds, aerosols, and distributions of gaseous species.

4.1. MRS Spectral Fitting

Zonally averaged MRS spectra (Section 2.5) were fitted using the NEMESIS optimal estimation retrieval algorithm (Irwin et al., 2008), which has been previously applied to Cassini/VIMS and Cassini/CIRS spectra of Saturn. Sources of spectral linedata and the generation of k-distributions were described on Section 3.1. Spectral uncertainties reported by the MRS pipeline (the ERR backplane) were averaged for the pixels used for each latitude, but were found to be unrealistically small—we retain the spectral shape of the uncertainty envelope, but increase the error by factors of 10–40 (depending on MIRI channel) to enable spectral fits with a goodness-of-fit of approximately one—this is the equivalent of adding forward-modeling uncertainty during the retrieval process (Irwin et al., 2008).

Given the broad spectral coverage, and the high spectral resolution, we adopted a multi-stage approach, first fitting undersampled broadband spectra to constrain atmospheric temperatures and aerosols, before fitting narrowband MRS spectra at their native sampling to study specific gaseous species. Each MRS subband was fitted simultaneously, but used the correct geometry (emission, incidence, and azimuthal angle) to calculate the atmospheric path, as small differences arise from different pointings between tiles and dithers. In addition, we divide the data at 7.3 μm, with longer wavelengths considering only thermal emission and no scattering, but shorter wavelengths considering multiple scattering of both reflected and thermal photons, as has been typical of Cassini studies (see Figure S7 in Supporting Information S1, which shows that aerosol-free models and cloudy, scattering models converge in the 6.6–7.3 μm range, although this is somewhat dependent on the choice of refractive indices described below). The sequential stages were as follows:

1. *Global Fit*: Fitting the full 7.3–16.3 μm region, sampling every fourth point in the spectrum to accelerate the retrieval process, to estimate the $T(p)$ profile as a function of latitude, along with initial assessments of gaseous variability. Temperatures, continuous profiles of ethane and acetylene, parameterized profiles of NH_3 and PH_3, and scaled abundances of C_2H_4, C_4H_2, C_3H_4, C_3H_8, C_6H_6, CH_3, and CO_2 were retrieved during step 1 (see below for discussion of priors). The gaseous abundances would be refined later, but this provided a first zonal-mean $T(p)$ structure. Tropospheric temperatures and gas abundances were determined by simultaneously fitting the H_2-He continuum observed beyond 15 μm and the absorption of NH_3 and PH_3 between 8 and 12 μm. Stratospheric temperatures are largely controlled by CH_4 emission at 7.8 μm, but also by the simultaneous fitting of temperature and composition from the ethane and acetylene emission. We omit wavelengths beyond 16.3 μm due to challenging fringing/ripples that dominate the long-wavelength spectrum, and the lack of an in-flight MRS calibration for channel 4 at the time of writing. We omit 11.9–12.3 μm due to a known artifact in this MRS subband, whereby light leaks through the MRS dichroic filter from 6.1 to 12.2 μm to create a source-dependent artifact in the data. This artifact was identified due to difficulties in fitting Saturn's C_2H_6 emission band at 12.2 μm simultaneously with CH_4 at 7.8 μm.

2. *Refined Temperatures*: The initial $T(p)$ from step 1 was then used as a prior for (a) a refined estimate of the stratospheric temperatures, using data from channels 1C and 2A (7.3–8.4 μm) at their full spectral resolution and (b) a refined estimate of tropospheric temperatures, ammonia, and phosphine from 8.0 to 11.5 μm (channels 2A to 2C). Examples of the quality of the spectral fits for latitudes at 20°N (representative of low latitudes) and 80°N (representative of the bright polar emission) are shown in Figures 11a and 11b.

Figure 10. Comparison of Cassini/CIRS observations in 2017 to Mid-Infrared Instrument/Medium Resolution Spectrometer (MIRI/MRS) observations in 2022. MRS spectra were convolved to the same spectral resolution as CIRS (15 cm^{-1}), and three CIRS northern hemisphere maps were zonally averaged onto a latitudinal grid. Brightness temperatures as a function of wavelength are shown in panels (a–c), showing stratospheric CH_4 emission on the left, ethane emission near 12 μm, and continuum H_2-He absorption on the right. In panel (d), the emission angles for MIRI (black) and CIRS (red) for each latitude are approximately the same, so differences are not due to limb brightening/darkening. CIRS measurements between ∼9–10 μm are disregarded (white rectangle) as they had low signal-to-noise.
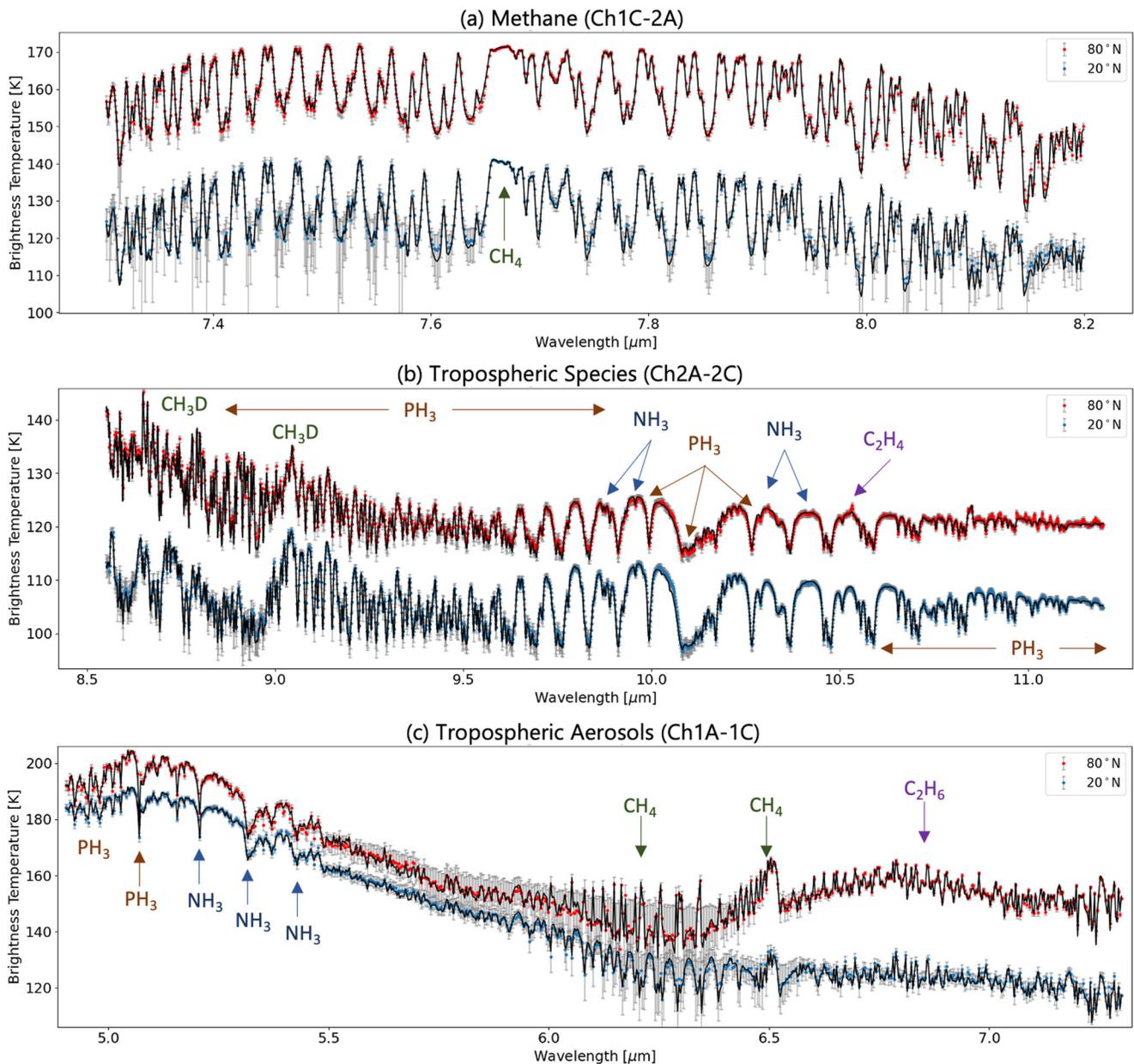
Figure 11. Examples of the quality of spectral fits (solid lines) to Mid-Infrared Instrument/Medium Resolution Spectrometer data (points with error bars) at different stages within our multi-stage retrieval. Panel (a) is dominated by stratospheric CH_4 emission, used to determine the vertical temperature structure; panel (b) sounds tropospheric species like PH_3, NH_3, and CH_3D; panel (c) sounds reflection and absorption by tropospheric aerosols, in addition to PH_3, NH_3, H_2O, and emission from stratospheric CH_4 and C_2H_2. Spectra at 80°N have been offset from the 20°N spectra by 20 K for clarity. Uncertainties are a scaled version of those reported by the JWST pipeline, as described in Section 4.

3. *Aerosol Fitting*: Temperatures were then fixed for aerosol and gaseous retrievals from the 4.9–7.3 μm range (channels 1A to 1C, sampling every third spectral point). Unlike the longer wavelengths, this region requires multiple scattering of reflected and thermal light to fit, and full details of the aerosol model are provided below, with example spectral fits shown in Figure 11c. The resulting aerosol profiles were then incorporated back into the initial temperature inversions to check for any changes in the $T(p)$ structure, using only their absorption cross-sections (i.e., without scattering). Changes to the resulting $T(p)$ were negligible, but would be dependent on the refractive indices of the aerosols, which are not uniquely constrained (see Section 4.3).

4. *Refined Composition*: Finally, we adopted the $T(p)$ and aerosol cross-sections, alongside the derived NH_3 and PH_3 distributions, as priors for focused retrievals of specific spectral features such as the hydrocarbons, HCN, CO_2, and H_2O. Examples for a range of gaseous species are shown in Figure 12, with key features labeled.
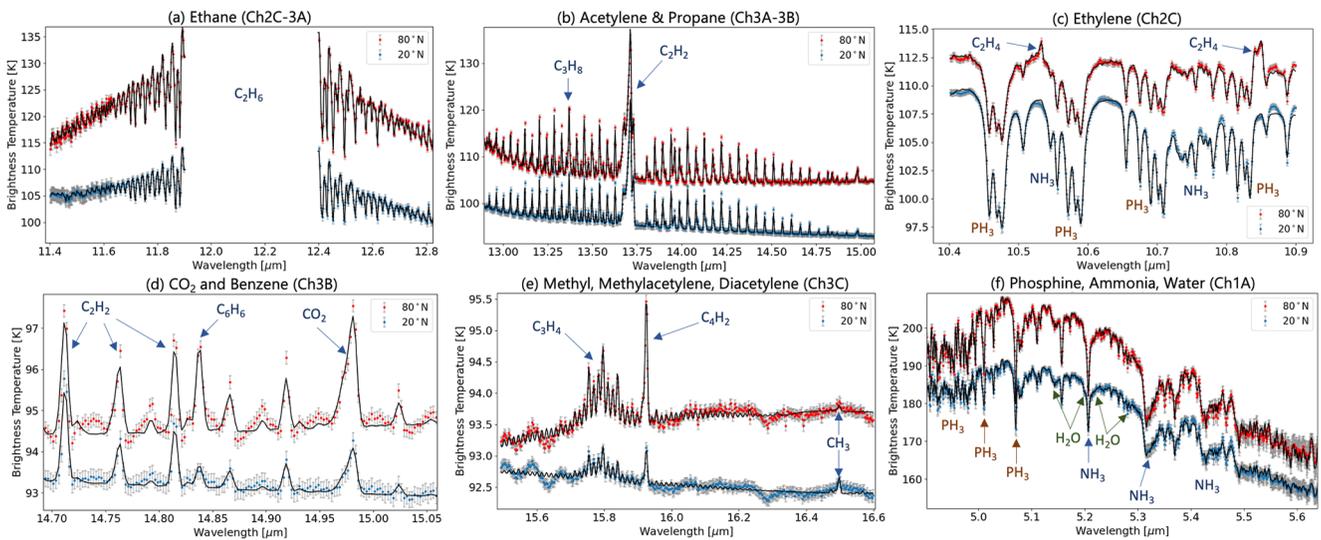
Figure 12. Example fits (black line) to observations (points with error bars) in specific regions of Saturn's spectrum, including those regions sensing stratospheric hydrocarbons (ethane in panel (a) with the central region omitted as described in the text; acetylene and propane in panel (b); ethylene in panel (c); CO_2 and benzene in panel (d); and methylacetylene, diacetylene, and methyl in panel (e)) and tropospheric absorptions from ammonia, phosphine, and (tentatively) water in panels (c, f). Spectra for 80°N have been offset from 20°N for clarity by 10 K in panels (a, c); 20 K in panels (b, f)—no offsets were used in panels (d, e).

4.2. Fitting Temperatures and Gases

Saturn's prior $T(p)$ at $p > 50$ mbar, as well as PH_3 and NH_3 profiles, are based on a low-latitude ($\pm 30°$ latitude) average from Cassini/CIRS nadir observations (Fletcher, Orton, Teanby, & Irwin, 2009). The $T(p)$ is extended deeper than 0.8 bar using a dry adiabatic lapse rate (Fletcher et al., 2011), and higher ($p < 50$ mbar) using a global average of Cassini/CIRS limb observations (Guerlet et al., 2009), resulting in a prior defined from 1 μbar to 10 bars. We adopt the He/H_2 ratio from Voyager (Conrath & Gautier, 2000), CH_4 and its isotopologues from Cassini/CIRS (Fletcher, Orton, Teanby, Irwin, & Bjoraker, 2009); C_2H_2, C_2H_6, and C_3H_8 from an average of CIRS limb measurements (Guerlet et al., 2009); all other hydrocarbons (C_2H_4, C_4H_2, C_3H_4, C_6H_6, CH_3), and CO_2 come from averages of the seasonal photochemical model of Moses and Greathouse (2005), updated to a finer latitude grid with zero meridional mixing ($K_{yy} = 0$ m^2/s, Moses et al., 2007). Prior deep abundances for CO (1.0 ppb, Noll & Larson, 1990), GeH_4 (0.4 ppb, Noll & Larson, 1990), H_2O (0.176 ppb, de Graauw et al., 1997), and AsH_3 (2.2 ppb, Fletcher et al., 2011) come from previous investigations at 5 μm. HCN uses the stratospheric upper limit from Herschel (22 ppb at $p < 1$ mbar, Fletcher et al., 2012).

With the exception of CO, AsH_3, and GeH_4, all species were allowed to vary from their priors during the MIRI/MRS retrievals. Depending on the size and strength of their spectral contributions in Figure 13, gases were either (a) retrieved as full, continuous profiles with height (C_2H_2, C_2H_6), (b) parameterized in terms of a deep mole fraction, transition pressure, fractional scale height (compared to the atmospheric scale height) up to the tropopause (NH_3, H_2O, and PH_3), or (c) simply scaled versions of the prior profiles (i.e., which implicitly assumes that the vertical profile is an accurate representation of Saturn's atmosphere). Contribution functions for these spectral ranges are shown in Figure 13, indicating the approximate sensitivity levels to which the different MRS channels are sensitive.

4.3. Fitting Aerosols

Saturn's aerosol distribution is best constrained via remote sensing at visible and near-infrared wavelengths, but the opacity, location, and wavelength-dependent scattering/absorption properties of aerosols contributes significantly in the MIRI/MRS range, particularly at wavelengths below 7.3 μm. Studies in this range remain somewhat limited, and are dominated by investigations of aerosol changes in discrete regions such as the polar domain (Sánchez-Lavega et al., 2020; Sromovsky et al., 2021) and the northern storm band (Sromovsky et al., 2013, 2016). Attempts to study the latitudinal distribution of aerosols have used Hubble (Pérez-Hoyos et al., 2016; Stam et al., 2001), Cassini/ISS (Roman et al., 2013), and Cassini/VIMS (Fletcher et al., 2011), with
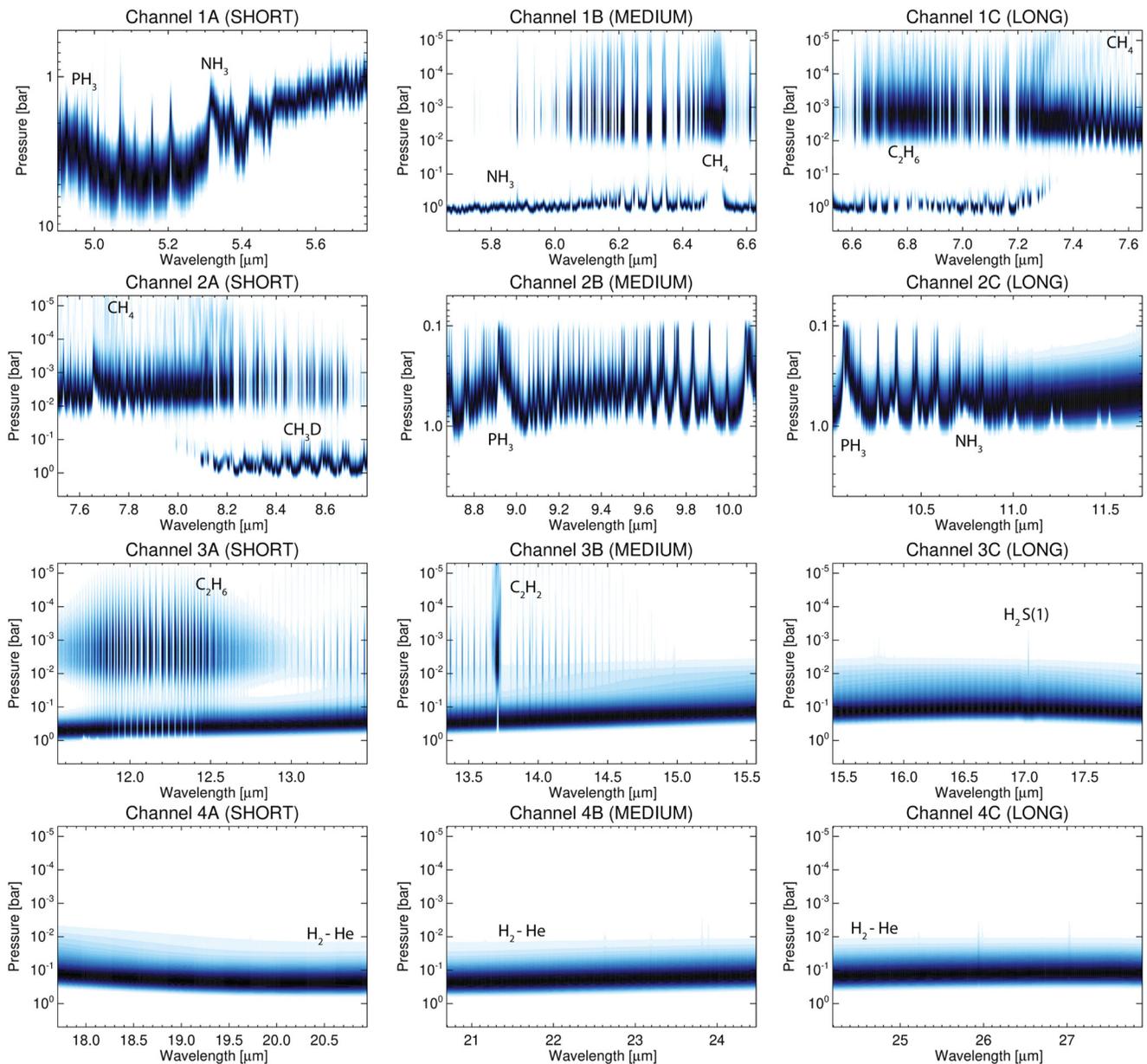
Figure 13. Cloud-free contribution functions (Jacobians showing the rate of change of spectral radiance with temperature) calculated for nadir viewing and a typical mid-latitude composition on Saturn. These contribution functions have been normalized at each wavelength, and darker shading indicates the greatest contribution. No aerosols are included in this model. Key gaseous features have been labeled, note that minor stratospheric species become apparent with higher emission angles (not shown). The y-axis changes in pressure range to emphasize dominant features.

the latter using only nightside 5-µm spectra to avoid the complications of reflected sunlight, whereas JWST/MIRI spectra are a blend of thermal emission and reflected sunlight. To our knowledge, there have been no aerosol retrieval studies that utilize the 5.1–6.8 µm domain inaccessible to Cassini.

Given the degeneracies inherent in fitting reflected sunlight spectra, as evidenced by the range of different results in the literature (Fletcher et al., 2020b), we initially adopted an Occam's-razor approach to fitting the 4.9–7.3 µm range. Figure 13 shows that the 5-µm region senses high pressures (3–7 bars) in the absence of aerosols, so we initially considered a single aerosol population near ~1.5 bars (i.e., above the primary contribution functions near 5.0–5.2 µm), rather than multiple different compact cloud decks, and allowed the base pressure, top pressure, total opacity, and vertical extension to vary freely during the fitting process. We also avoided imposing any particular spectral shape to the aerosol cross-section, single-scattering albedo, and phase functions (modeled via two-term

Henyey Greenstein functions fitting the results of Mie scattering calculations). Values for particle radius (from a standard gamma distribution with a 5% variance) and the spectrally uniform real and imaginary refractive indices were chosen after tests at several latitudes where these values were allowed to vary freely. The radius had a small effect, with $r = 1.0 \pm 0.05$ μm selected as a best fit. The spectral fits were largely insensitive to the real refractive index, with values representative of NH$_3$ ice $n_r \sim 1.4$ (Martonchik et al., 1984) and NH$_4$SH solid $n_r \sim 2.3$ (Howett et al., 2007) fitting equally well, so a mean $n_r = 1.8$ was selected. The most important parameter was the imaginary refractive index n_i, which varies considerably in the infrared depending on the assumed composition of the aerosols. Fits were significantly improved with smaller values of n_i in the 5-μm region than would be typically expected for "pure" NH$_3$ and NH4SH aerosols - the final selected value was $n_i = 1 \times 10^{-3}$ over the whole range, resulting in weakly absorbing particles (single scattering albedoes >0.95 in this spectral range).

We attempted to fit the 4.9–7.3 μm range (step 3, above) using this single-cloud layer and the choices of optical properties described above. Retrievals with multiple scattering of reflected and thermal photons are numerically intensive, requiring numerical evaluation of Jacobians at each step of the inversion, so MIRI/MRS spectra from channels 1A, 1B, and 1C were undersampled by a factor of 4 to ensure a good fit across the whole 4.9–7.3 μm range. The latitudinally resolved $T(p)$ derived from steps 1 and 2 of our retrieval scheme were required to correctly reproduce emission from the CH$_4$ ν_2 band at 6.5 μm and the C$_2$H$_6$ emission band at 6.8 μm, seen in Figure 11c, particularly at high-latitudes where emission from the warm NPSV dominates. We varied the vertical location and extent of the cloud simultaneously with parametric profiles of NH$_3$, PH$_3$, and H$_2$O.

This single-cloud model was remarkably successful in fitting most of the 4.9–7.3 μm range, allowing us to then search for discrepancies which might hint at more complicated cloud structure, such as the multi-layer clouds of Sromovsky et al. (2021), or the potential wavelength-dependent absorptions of photochemical hazes such as those of Guerlet et al. (2015). Poor fits in the dark equatorial band and polar latitudes led us to experiment with a second cloud layer in the upper troposphere sitting at higher altitudes than the original layer, providing further degrees of freedom but informed by the observation of hazes in Saturn's upper troposphere (Roman et al., 2013). A real refractive index of $n_r = 1.74$ was selected, similar to the value for diphosphine at 195 K (P$_2$H$_4$) that had been adopted in Cassini/VIMS studies of upper-tropospheric hazes (Sromovsky et al., 2021), based on the expected photochemical production from PH$_3$. The resulting fits were weakly sensitive to the aerosol radius (1.0 ± 0.05 μm was selected) and imaginary refractive index ($n_i = 5 \times 10^{-3}$ was selected). This double-cloud scheme can be thought of as representing the upper tropospheric haze and the top-most condensate cloud, with their base pressures, opacities, and vertical extensions all freely varying during the 4.9–7.3 μm fitting, and producing the high-quality fits shown in Figure 11c. The results will be discussed in Section 5.

Finally, although Cassini/CIRS observed aromatic and aliphatic hydrocarbon aerosols in the polar stratosphere ($p < 8$ mbar) in limb observations (Guerlet et al., 2015), there is limited need to include them in the nadir MIRI/MRS spectral fitting. The CIRS results suggested a peak in opacity near 6.9 ± 0.3 μm, and there is a subtle but compelling residual in the spectral fits in the same location (see Figure S5 in Supporting Information S1), which will be the topic of future investigations.

5. Saturn's Temperatures, Aerosols, and Composition in 2022

The results of the multi-stage retrievals of zonally averaged temperatures, aerosols, and gaseous species are described in the following subsections.

5.1. Temperatures and Winds

Saturn's zonal-mean temperatures during northern summer are shown in Figure 14, as derived from step two (i.e., refined spectral fitting at full spectral resolution after a "global fit" to the 7.3–16.4 μm spectrum). The temperature inversion confirms many of the conclusions available from the brightness temperature maps alone. The troposphere is characterized by a cool EZ; temperature gradients between mid-latitude belts and zones that correlate with the peaks of the cloud-tracked zonal winds; and a warm polar domain. The cool EZ is coincident with the highest aerosol opacity (Section 5.2), and it is therefore possible that our aerosol-free assumption for wavelengths beyond 7.3 μm is inadequate, despite tests in Section 4 suggesting that the derived aerosols had minimal absorption at these wavelengths. Further refinement of the aerosol refractive indices, incorporating wavelengths longer than 7.3 μm, would be needed to fully resolve this potential degeneracy between aerosols and temperatures.
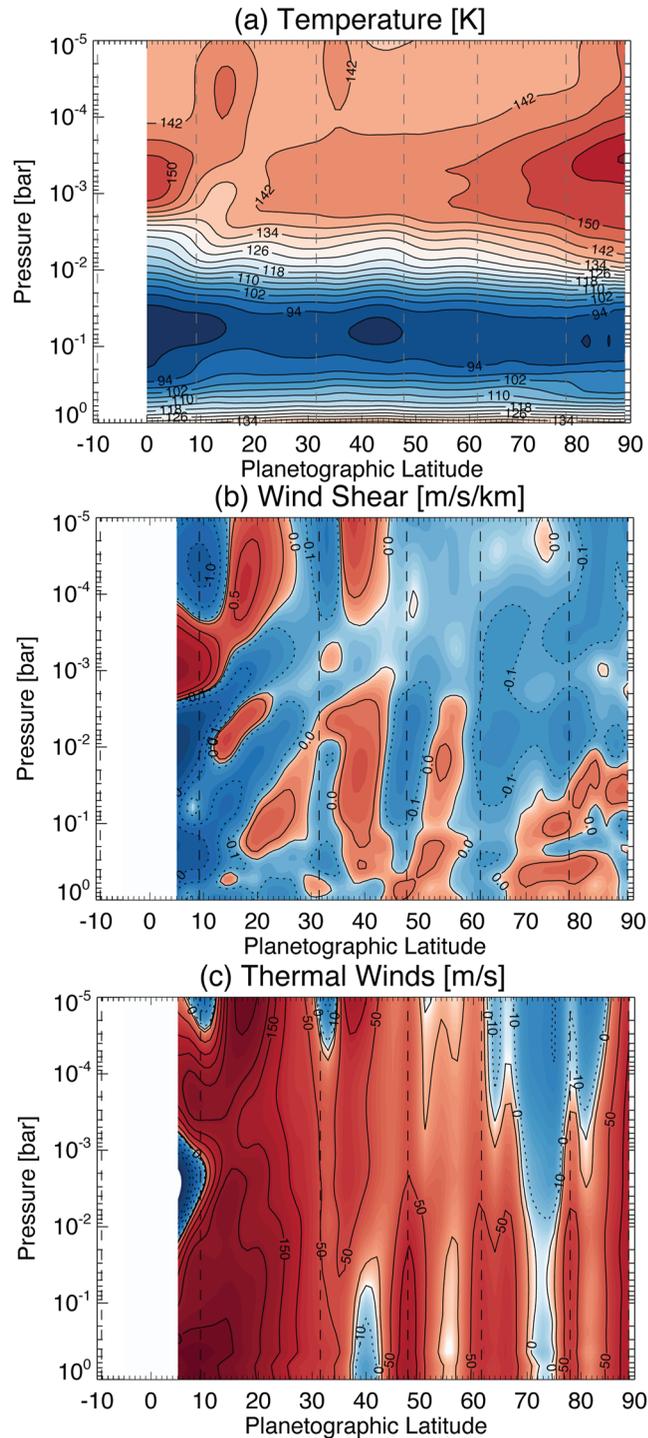
Figure 14. Temperatures, windshear, and thermal winds as a function of latitude derived from Mid-Infrared Instrument/Medium Resolution Spectrometer spectroscopy. The peaks of cloud-tracked eastward winds are shown as vertical dashed lines for context. In panels (b, c), regions of negative windshear/westward winds are shown as blue with dotted contours; regions of positive windshear/eastward winds are shown as red with solid contours. Temperature contours are every 4 K; windshear and wind contours are logarithmic to show structure, but windshears are labeled at ± 0.1, ± 0.5, and ± 1.0 m/s/km; winds are labeled at 10, 50, 100, 150, and 200 m/s. Absolute values for derived thermal winds are subject to significant uncertainties related to the integration of the thermal wind equation (Fletcher et al., 2016), so should be used as a guideline to trends only.

The stratosphere exhibits warming within the polar domain, reaching maximum temperatures of 154 ± 1 K within the NPSV (poleward of 78°N) and 160 ± 2 K within the NPC (poleward of 87°N). These peak temperatures are only slightly cooler than those observed within the southern stratosphere in 2004–2005—the SPSV and SPC—by Cassini/CIRS (Fletcher et al., 2018b), a seasonal asymmetry possibly due to Saturn's orbital eccentricity. Radiative models demonstrate that the bulk of this warming is driven by seasonal radiative heating (Blake et al., 2022; Guerlet et al., 2014; Hue et al., 2016), but the sharp boundaries are related to dynamics (e.g., stratospheric winds encircling the NPSV and NPC). Temperature inversions indicate a moderate stratospheric cooling at pressures below 300 μbar, with temperatures approaching a 140 ± 3 K quasi-isothermal structure up to the base of the thermosphere. While retrieved low-pressure temperatures are somewhat influenced by the choice of prior, this isothermal structure is consistent with radiative modeling (e.g., Guerlet et al., 2014).

The most prominent feature of the MIRI temperature field is the vertical structure of Saturn's Equatorial Stratospheric Oscillation (we refer to this as the SESO, as the semi-annual nature of the oscillation is questionable). During the November-2022 phase, a prominent warm anomaly (153 ± 0.8 K) is observed between the equator and ~10°N centred near 0.7 mbar. This is some 12–14 K warmer than temperatures at 0.1 mbar, and is responsible for the warm band of bright stratospheric emission observed in Figures 7 and 8. This is accompanied by off-equatorial temperature maxima near 13°N, a strong warm anomaly near 0.05 mbar, and a weaker cool anomaly near 1 mbar. Similar vertical patterns were observed ~16–17 years earlier by Cassini/CIRS limb spectroscopy (Fouchet et al., 2008) in 2005–2006, and are revealed here due to the high spectral resolution of MIRI/MRS.

Latitudinal temperature gradients dT/dy (where y is the north-south distance in km) are converted to vertical windshears du/dz (where z is altitude) via the thermal wind equation (e.g., Holton, 2004), omitting the equatorial region where the Coriolis parameter tends to zero. These are shown in Figure 14b, and show intriguing shear structure equatorward of 30°N (broadly the domain occupied by Saturn's equatorial jet). The positive equatorial shearzone in near 1 mbar in 2022 is likely to be the one that was seen near 0.1–0.3 mbar in 2017 by Cassini (Fletcher et al., 2017), having descended over a decade in pressure in 5 years. Positive and negative shear zones associated with the SESO and its off-equatorial structures appear to move diagonally to higher pressures with decreasing latitude. For example, the negative shear zone in the upper troposphere appears continuously connected to the negative shear zone at 1 mbar and 30°N. The same connection is seen for the negative shear zone at 10 mbar (5°N) and 0.05 mbar (30°N). Such a system of stacked shear zones connecting the equator and off-equatorial features was nicely captured by the model of Bardet et al. (2022).

Windshears derived from nadir infrared data provide a good picture of the shearzones as a function of altitude and latitude, but using them to integrate winds with altitude and across regions of low information content (e.g., the tropopause and lower stratosphere) can generate significant uncertainties (e.g., Fletcher et al., 2016; Fouchet et al., 2008). Nevertheless, we display the estimated thermal winds in Figure 14c, assuming that the continuum-band winds measured by García-Melendo et al. (2011) are placed at 500 mbar. Treating these thermal winds with appropriate caution, we infer a localized equatorial westward jet (exceeding −200 m/s near 1–5 mbar and equatorward of 10°N, embedded within a larger region of eastward flow that spans the tropics equatorward of 30°N. The westward jet is below an eastward equatorial jet (~200 m/s) near 0.1–0.5 mbar, with the peak-to-peak contrast of ~400 m/s between eastward and westward maxima being comparable to that derived from Cassini limb observations (Fouchet et al., 2008). Direct observations of Saturn's stratospheric winds by ALMA (Benmahi et al., 2022) four years earlier (2018) observed a ~300 m/s eastward jet between 20°S and 20°N but with a coarse vertical resolution, covering 0.01–20 mbar. Although this is qualitatively consistent with the broad eastward flow inferred from MIRI in Figure 14c, the coarse resolution of the ALMA data may average over any oscillatory wind patterns over a decade of pressure. Alternatively, differences between ALMA and MIRI might simply reflect the downward propagation of these stacked zonal jets over 4 years, and future joint campaigns between ALMA and JWST would be welcome to confirm this, alongside ground-based spectroscopic monitoring of the equatorial CH_4 emission at high spatial and spectral resolution.

Beyond the equator, the correlation between dT/dy and the cloud-tracked zonal winds causes the decay of the cloud top winds with height (e.g., the westward jet near 42°N becomes eastward at $p < 80$ mbar), as previously observed by Cassini (Read et al., 2009). Finally, the strong dT/dy at the edge of the NPSV implies negative windshear and the inference of westward flow around the edge of the vortex for $p < 10$ mbar (Fletcher et al., 2018b), at a latitude consistent with the westward winds directly observed by ALMA near 74°N planetographic (Benmahi et al., 2022). This westward wind is zonally symmetric and in balance with the seasonal temperature gradients from radiative heating within the NPSV.
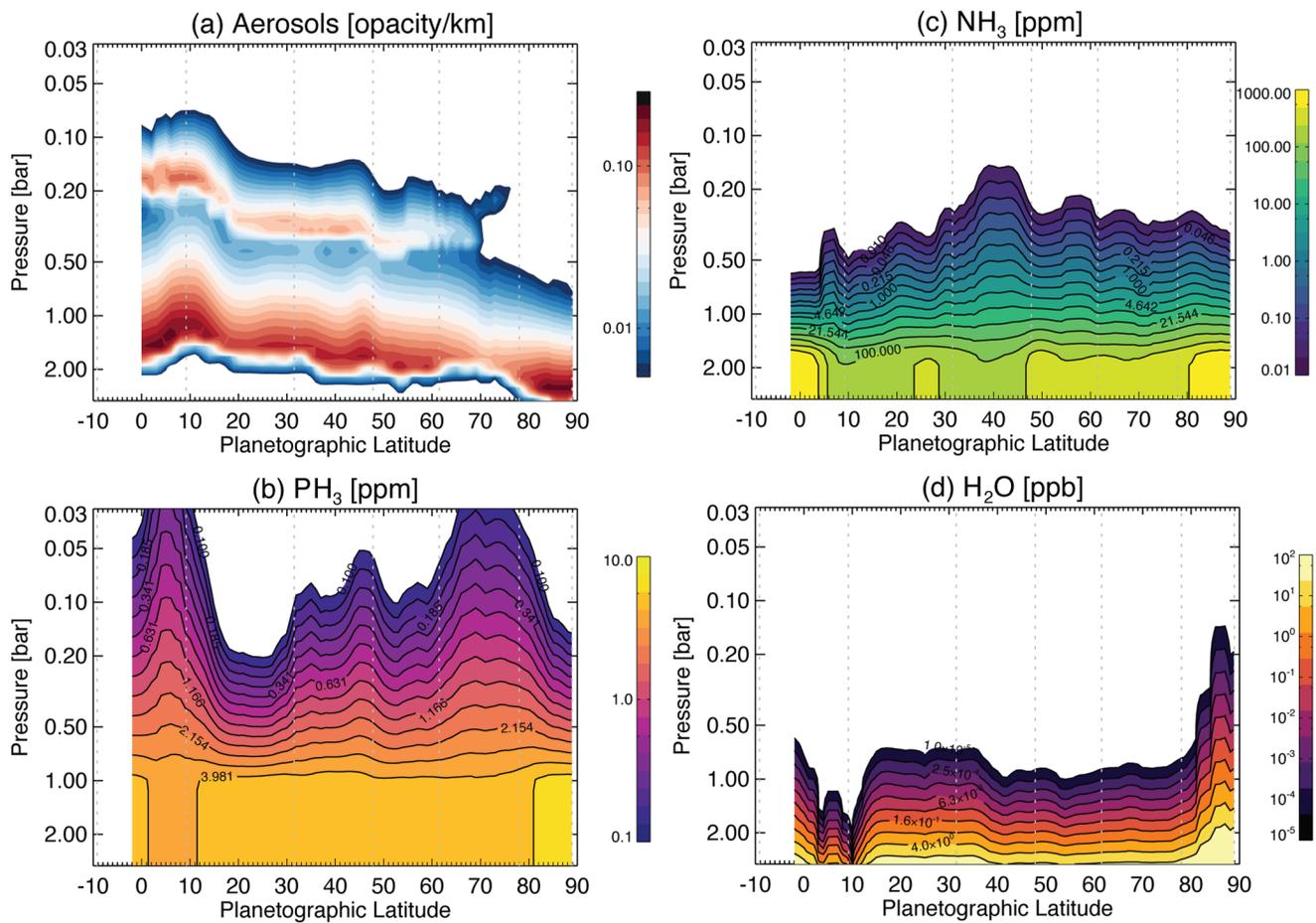
Figure 15. Aerosols, phosphine, ammonia, and water derived from the 4.9–7.3 μm region. Aerosols in panel (a) are plotted in opacity/km at a reference wavelength of 5 μm, calculated following the scheme in Appendix C of Irwin et al. (2022). A logarithmic color bar is used to show structure within the aerosol cross-section. For the gases in panels (b–d), the contours are also logarithmic to allow for the rapid decline of the abundance with altitude. PH_3 and NH_3 are provided in ppm, H_2O is given in ppb. Vertical dotted lines show the latitudes of tropospheric eastward jets.

5.2. Aerosols

The zonal-mean distribution of Saturn's aerosols are shown in Figure 15a, derived from fits to the 4.9–7.3 μm region using the double-cloud scheme and multiple scattering of reflected and thermal photons as outlined in Section 4.3. Although significant degeneracy exists in the choices of aerosol refractive indices and size distributions, the need for two clouds was evident from the difficulty fitting equatorial latitudes (where clouds are most reflective). The base pressures, vertical extensions, top-most pressures, and total opacity were then varied as free parameters for the two aerosol populations, resulting in the stacked cloud decks observed here.

The upper cloud, which may comprise a photochemically produced haze potentially associated with diphosphine (Ferris & Benson, 1980), is optically thickest, highest (a base near 200 mbar), and most extended at the equator, reaching into the lower stratosphere near 60–70 mbar. This upper haze is found deeper (near 300 mbar) and more compact from 18°–48°N, and then declines considerably at higher latitudes beyond 60°N. The latitudinal dependence and altitude of this haze layer is well-matched to the small inflection in the $T(p)$ profile observed by Cassini/CIRS and known as the "temperature knee" (Fletcher et al., 2020b), suggesting that seasonal heating of this aerosol population is responsible for the change in the curvature of the vertical temperature profile. The absence of this aerosol at high latitudes may be partially responsible for the bright 5-μm emission between 60° and 80°N in Figures 7, 8, and 9. The latitudinal distribution of this upper haze also matches that derived from Palomar visible-light observations acquired in 1995 (Stam et al., 2001), and Cassini/ISS determinations of aerosols during 2004–2007 (Roman et al., 2013), which identified haze-top pressures ranging from 40 to 150 mbar, with the thickest and highest at the equator, becoming deeper and thinner at mid-latitudes.

The deeper cloud, which may be associated with condensates of NH_3 (potentially coated in other material, e.g., Sromovsky et al., 2021), resides between 1 and 2 bars, but with an extension to lower pressures that maybe merges with the upper haze. The base pressure of this cloud varies with latitude, reaching the lowest pressures (1.2 bars) near 10°N, which was the site of the highest reflectivity in Figure 9, and the deepest pressure (2.6 bars) within the polar domain. Indeed, the inversions poleward of 78°N suggest that this deep cloud resides at $p > 2$ bars and is vertically compact, responsible for both the dark thermal emission at 5 μm and the absence of reflectivity at 5.2 μm—the dark north pole is therefore caused by this deep aerosol layer. The compact nature of this cloud deck appears to be consistent with Cassini observations (Fletcher et al., 2011; Sromovsky et al., 2021), although we caution that the vertical extension is a rather poorly constrained parameter in these retrievals. The mean pressure of the cloud base is again consistent with that found by Cassini/ISS (1.75 ± 0.4 bars, Roman et al., 2013), even though optical measurements only reveal this deep cloud when there are gaps in the overlying haze.

This simple two-cloud scheme does not provide constraints on two other proposed cloud layers: neither a deep cloud (2.7–4.5 bars, potentially due to NH_4SH Sromovsky et al., 2021); nor the stratospheric hazes (near 50 mbar, Guerlet et al., 2015; Roman et al., 2013; Sromovsky et al., 2021). The deep cloud does not seem to be required to reproduce the MIRI data, but this may be due to lack of constraint from reflected sunlight at shorter wavelengths (e.g., from NIRSpec). The very low opacities (0.08 ± 0.05 at 619 nm) and small particle sizes (<0.3 μm) of the stratospheric aerosols inferred by Roman et al. (2013) make it very unlikely that they would contribute significant opacity at longer mid-IR wavelengths. Nevertheless, very subtle residuals in our fits to north polar latitudes near 6.8 ± 0.2 μm could be related to the stratospheric aerosols (see Figure S5c in Supporting Information S1), and will be the topic of future studies, given their photochemical nature and potential importance in the balance of radiative heating and cooling in the polar domain (Guerlet et al., 2015).

5.3. Tropospheric Gases

Saturn's tropospheric gases—namely NH_3, PH_3, and H_2O—are accessible in the 4.9–6.0 μm region (primarily channel 1A) and the 8–11 μm region (spanning channels 2A to 2C). The latter sounds higher altitudes in the upper troposphere, whereas the former provides access to the deeper cloud-forming layers.

5.3.1. Phosphine

Phosphine (PH_3) is retrieved parametrically from both spectral regions (i.e., varying the deep mole fraction and scale height for a fixed transition pressure of 1 bar), and the results from 5 μm are shown in Figure 15b. For $p > 1$ bar, the deep abundance varies between 4.0 and 5.0 ppm over most of the northern hemisphere, consistent with results from Cassini/VIMS (Fletcher et al., 2011; Sromovsky et al., 2021), but with no notable contrasts at the equator, and a higher abundance 6.5 ± 1.0 ppm poleward of 80°N. Much of the latitudinal structure is therefore found in the upper troposphere, driven by the fractional scale height of the gas. For $p < 1$ bar, PH_3 is enriched equatorward of 15°N with evidence for a slight depletion right at the equator. Further enriched bands are found at 33°N, 46°N and between 60° and 80°N, with a general decline in abundance toward the north pole. The equatorial peak and presence of bands of elevated PH_3 were also observed by Cassini/CIRS (Fletcher, Orton, Teanby, & Irwin, 2009), but the precise locations differ—in particular, there is no good correspondence between mid-latitude PH_3 bands and zones of cooler temperatures, as we might expect if only dynamics (i.e., upwelling) were controlling the mid-latitude distribution. Conversely, there is a good correspondence between higher cloud bases and the elevated PH_3, reinforcing links between PH_3 and aerosols shielding the gas from UV photolysis. This correspondence breaks down in the 5-μm-bright band near 60°–80°N, where we have thin clouds but enriched PH_3, suggesting a more complex balance between aerosol shielding and vertical mixing. Where clouds are deepest and most compact poleward of 80°N, PH_3 could be depleted either by polar subsidence (Fletcher et al., 2008) or by diminished aerosol shielding.

Inversions from the 10-μm region show a similar morphological structure but primarily sense $p < 1$ bar (see Figure 13). However, the mid-latitude peaks are at different locations—29° and 44°N, and the deep abundances vary between 7 and 10 ppm, a factor of ~2 higher than those derived from the 5-μm region. This is a known discrepancy between PH_3 abundances derived from the two regions and occurs on both Saturn (Fletcher et al., 2011) and Jupiter (Giles et al., 2015), and reconciliation will require joint fitting of both spectral domains with multiply scattering aerosols.

5.3.2. Ammonia

The latitudinal distribution of NH_3 was also retrieved parametrically (with a transition pressure at 1.75 bars), with the 5-μm results shown in Figure 15c. As previously observed by Cassini/RADAR (Laraia et al., 2013) and

VIMS (Fletcher et al., 2011), MIRI reveals a strong equatorial enhancement within 5° of the equator, with deep abundances below $p > 1.75$ bars of 450–650 ppm, compared to a minimum of ~150 ppm at 10°N. This equatorial enhancement on Saturn shares similarities with that observed on Jupiter (de Pater et al., 2016; Li et al., 2017), and suggests shared dynamics driving the unique compositions of their cold Equatorial Zones, compared to strong NH_3 depletion at other latitudes. Despite the strong equatorial maximum at depth, the abundance falls steeply with height equatorward of 20°N, such that NH_3 at the 200-mbar level displays a local equatorial minimum, perhaps due to the enhanced condensation through cold equatorial temperatures to form the thicker clouds observed here.

Further local maxima in the deep abundance occur at 26° and 49°N, which are similar in size (but at different latitudes) compared to peaks observed by Cassini/VIMS in 2006 (Fletcher et al., 2011), suggesting temporal variability in the abundance of NH_3 in the mid-latitude bands. The region near 40°N is notable as displaying the shallowest gradient in NH_3 for $p < 1$ bar, coinciding with the coldest tropospheric band in Figure 14a, but is actually a local minimum (~100 ppm) in the deep NH_3 abundance for $p > 1.75$ bars. Similarly, there is a general increase in deep abundance toward the polar domain (~600 ppm for $p > 1.75$ bars), but also a shallower upper tropospheric gradient implying a local polar minimum at 200 mbar. These MIRI results imply that ammonia displays different latitudinal distributions above and below the condensed aerosols near 1.75 bars, suggestive of differing circulation patterns at different heights (Fletcher et al., 2020a). To reinforce this, NH_3 was also retrieved from the 10-μm region, sensing higher altitudes of the upper troposphere, and resulted in a relatively meridionally uniform distribution similar to that derived by Cassini/CIRS (Hurley et al., 2012). The strongest NH_3 contrasts are therefore only seen in the cloud-forming region sensed near 5 μm, with only small latitudinal gradients in the stably stratified upper troposphere sensed near 10 μm.

5.3.3. Water

Perhaps the most tantalizing prospect offered by MIRI/MRS is the possibility of mapping Saturn's tropospheric water in the 5.1–5.5 μm region, which remained out of reach to Cassini/VIMS because of the lack of spectral coverage beyond 5.1 μm. de Graauw et al. (1997) detected Saturn's tropospheric water with disc-averaged observations from ISO/SWS, fitting it with 0.2 ppm at $p > 3$ bars and generally sub-saturated conditions. H_2O was retrieved parametrically, with initial testing at mid-latitudes suggesting the transition pressure should lie at $p > 4$ bars (5 bars was chosen), a weak sensitivity to the chosen deep abundance (10 ppm was selected), but a stronger sensitivity to the fractional scale height, so only the latter parameter was allowed to vary.

Tropospheric water lines are difficult to observe between the forest of PH_3 features in Figure 11f, and are most visible as small notches either side of the narrow NH_3 feature near 5.2 μm. These H_2O features are present at all latitudes, but are close to the level of the spectral residuals seen elsewhere in the channel-1 data (see Figure S5c in Supporting Information S1). Nevertheless, the MIRI/MRS data provide tentative evidence of latitudinal variability of H_2O in Figure 15d. At 3.3 bars, the water abundance varies from a maximum of ~200 ppb right at the equator (consistent with ISO estimates from de Graauw et al., 1997), to ~10 ppb between 5° and 10°N, to ~145 ppb from 15° and 35°N, then declines to ~80 ppb from 40° and 80°N. Poleward of 15°N, the changes in abundance with latitude mirror those in the aerosol distribution, with a tendency for enhanced H_2O where the aerosols have a higher optical depth, although we caution that this could reflect a model-dependent degeneracy given the weakness of the H_2O features. The low values near 5°N are very poorly constrained due to the thicker aerosol opacity, but are possibly due to enhanced condensation in the cool EZ. The shallower gradient in the polar domain are possibly due to the warmer upper-tropospheric temperatures there and the absence of upper tropospheric aerosols, but the same is not seen for NH_3. Conversely, the increase in H_2O right at the equator mimics the equatorial column of NH_3, suggesting a volatile-rich domain at Saturn's equator.

We note that the challenge of calibrating MRS channel 4 (i.e., beyond 18 μm) limits our sensitivity to the distribution of stratospheric H_2O, which will be the topic of future investigations.

5.4. Stratospheric Chemistry

The spatial distribution of chemical species provides a means to trace Saturn's stratospheric circulation, to understand the photochemical lifetimes of different products, the exogenic supply of oxygenated species, and the potential influence of ionisation on the chemistry of the polar domains. As described in Section 3.1, MIRI/MRS provides access to a host of stratospheric chemicals with a higher spectral resolution and sensitivity than Cassini/CIRS. However, fringing artifacts that still plague wavelengths beyond 10 μm make precise quantitative
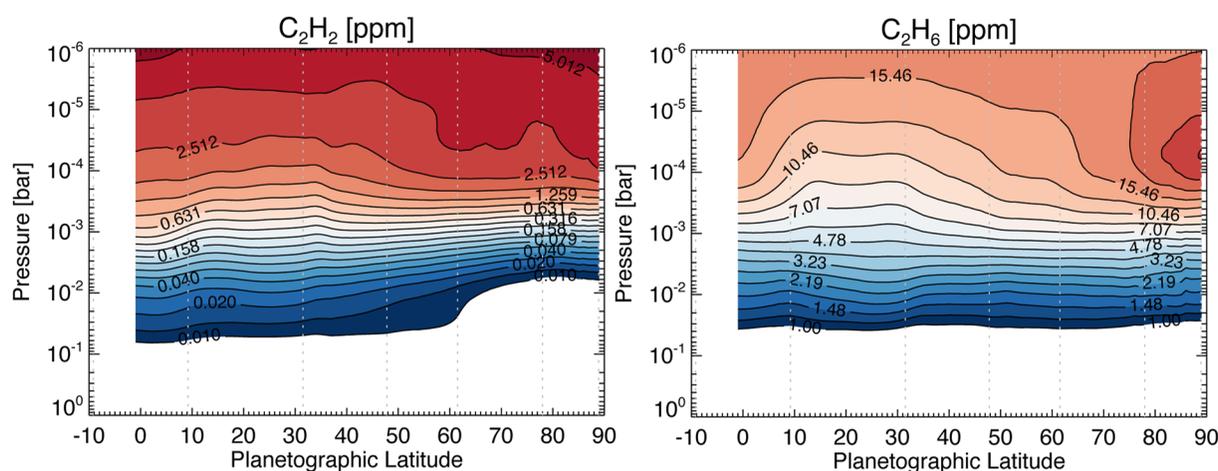
Figure 16. Distributions of acetylene and ethane, derived as continuous profiles to capture changes in the vertical gradients of these species. Contours are logarithmic, and labeled in ppmv. Vertical dotted lines show the latitudes of tropospheric eastward jets. A cross-section at 0.5 mbar is shown in Figure 17.

measurements challenging, particular for minor species. In the following sections, we present an initial assay of Saturn's stratospheric composition based on MIRI/MRS data.
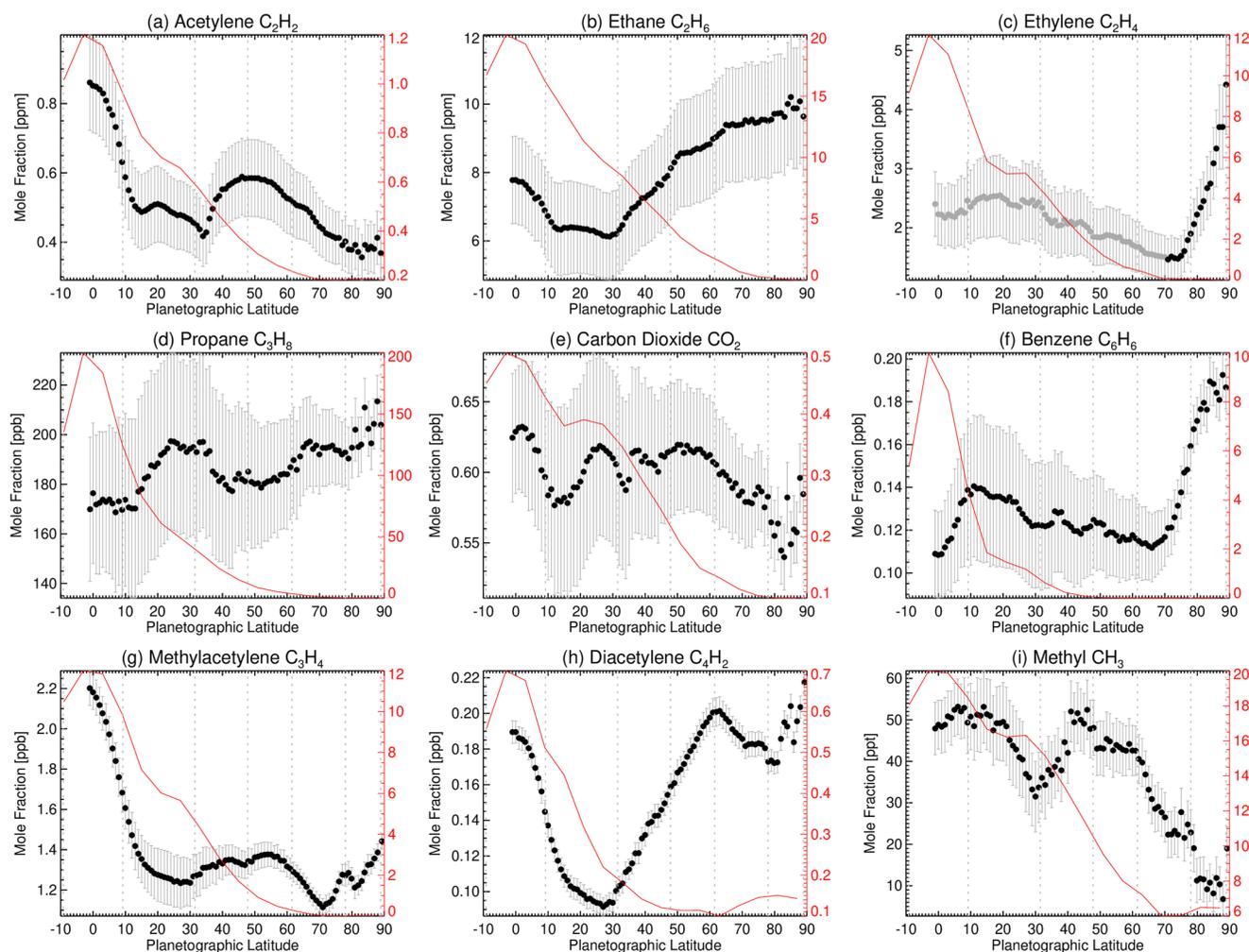
5.4.1. Acetylene and Ethane

Latitudinal cross-sections of ethane (C_2H_6) and acetylene (C_2H_2) are shown in Figure 16, and at the 0.5-mbar level in Figures 17a and 17b, based on spectral fits shown in Figure 12. Cassini observations revealed that both species are time-variable, responding to Saturn's seasonally evolving circulation and solar flux. The equator-to-pole gradient of C_2H_2 changes with height, with the upper stratosphere showing polar enrichment (poleward of 60°N and $p < 0.1$ mbar), but the lower stratosphere showing polar depletion ($p > 0.1$ mbar) due to the stronger gradient of C_2H_2 near the poles compared to at other latitudes. C_2H_6 also shows strong polar enrichment (poleward of 78°N and $p < 0.1$ mbar, within the NPSV). Both species show enhancements at the equator, as previously observed by Cassini (Guerlet et al., 2009; Sinclair et al., 2013; Sylvestre et al., 2015) and predicted by photochemical models based on the annual-average insolation (Hue et al., 2015; Moses & Greathouse, 2005), but this too is time variable, with evidence that the equatorial C_2H_6 peak has strengthened with time whereas C_2H_2 has remained reasonably constant (Fletcher et al., 2020b).

The different latitudinal trends in the lower stratosphere (C_2H_2 declining toward high latitudes, C_2H_6 increasing) have been observed previously, with short-lived C_2H_2 more closely following photochemical predictions of Moses and Greathouse (2005) (Figure 17a), whereas long-lived C_2H_6 is more sensitive to stratospheric circulation. Intriguingly, local maxima between 10° and 30°N observed in both species during northern winter by Cassini (2005–2012, Guerlet et al., 2009; Sylvestre et al., 2015) have now been replaced by local minima between 10° and 35°N during northern summer observed by JWST. This supports the idea that wintertime subsidence has been replaced by summertime upwelling in this latitude range (i.e., upwelling of hydrocarbon-depleted air from the lower stratosphere), associated with the seasonal reversal of the inter-hemispheric Hadley cell (Bardet et al., 2022; Friedson & Moses, 2012). This upwelling may provide an explanation for why MIRI observed colder stratospheric temperatures in 2022 (Section 5.1) compared to Cassini in 2017.

5.4.2. Ethylene

Ethylene was previously only detected within Saturn's storm-perturbed stratosphere (Hesman et al., 2012; Moses et al., 2015), due to the elevated temperatures and a photochemical increase in the C_2H_4 abundance in 2011. Other than the storm and a reported ground-based detection (Bézard et al., 2001b), C_2H_4 had proven elusive until the high sensitivity of MIRI/MRS, which reveals 10.5-μm C_2H_4 emission within the NPSV for the first time (Figure 17c, 0.5-mbar abundances of 4.0 ± 0.5 ppb poleward of 80°N). This abundance is a factor of 2–3× lower than that expected (but not seen) at the equator due to neutral photochemistry (Moses & Greathouse, 2005). Note that the emission features are only readily detectable in spectra poleward of 70°N—at lower latitudes, our model provides the highest C_2H_4 abundance that would be consistent with the non-detection of emission (within

Figure 17. Distributions of stratospheric species at 0.5 mbar: acetylene, ethane, ethylene, propane, CO_2, benzene, methyacetylene (propyne), diacetylene (1,3-butadiyne), and methyl in Saturn's northern summer, compared to the predictions of the neutral photochemistry model for $L_s = 150°$ (Moses & Greathouse, 2005; Moses et al., 2007). The photochemical model is shown in red, and is referenced to the right-hand axis so that both the shape of the distribution and differences in absolute abundances can be compared. Error bars are shown in gray, but these do not include uncertainties due to scaling a latitudinally uniform a priori profile. If the shape of the profile changes significantly with latitude (as is expected for benzene and C_4H_2 from previous studies), this could influence the retrieved values. Vertical dotted lines show the latitudes of tropospheric eastward jets. Gases in panels (a–c) were derived as full vertical profiles, other gases are derived as scale factors for our a priori profiles. Gray points in panel (c) signify a lack of obvious detection of C_2H_4 emission by eye.

uncertainties). The seasonal model overpredicts the estimated low-latitude abundance (2.3 ± 0.5 ppb at 0.5 mbar compared to ~12 ppb from the model) by a factor of 4, but the data are more consistent with updated models for Saturn's stratosphere (1–2 ppb at 0.5 mbar from Figure 6 of Moses et al. (2015)).

Nevertheless, the polar maximum in C_2H_4 in Figure 17c is unexpected on the grounds of neutral photochemistry, and is suggestive of either subsidence of hydrocarbon-rich air from higher altitudes (leading to the maxima in ethane and acetylene), or due to an enhanced contribution from ion-neutral chemistry at the highest latitudes. Distinguishing these scenarios will require future modeling work for the chemistry of the NPSV.

5.4.3. C_3, C_4, and C_6 Hydrocarbons

Propane is detected as a perturbation to the stronger C_2H_2 lines near 13.37 μm (indicated in Figure 12), which results in the large uncertainties on the distribution in Figure 17d. Propane bands ν_{20} and ν_{21} are observed near 9.4 and 10.7 μm, respectively (see Figure S6 in Supporting Information S1), but primarily at high latitudes. The strongest detections are within the warm NPSV, with abundances near 200 ± 10 ppb, and a relatively uniform distribution with latitude, consistent with that found by Sylvestre et al. (2015). It is clear that C_3H_8 does not follow

the predictions of seasonal photochemistry, suggesting the influence of meridional circulation on the distribution of long-lived propane (e.g., similar to the argument for C_2H_6, Moses & Greathouse, 2005).

Unlike propane and ethane, the unsaturated hydrocarbons *methylacetylene* (C_3H_4) and *diacetylene* (C_4H_2) are relatively short-lived species that track the photochemical model predictions at latitudes equatorward of 45°N, with C_3H_4 in particular showing the expected equator-to-pole contrast in Figure 17g. C_4H_2 shows a local minimum near 20°–40°N that has evolved from the local maximum observed by Cassini in 2005–2006 (Guerlet et al., 2010), possibly related to the onset of low-latitude stratospheric upwelling during northern summer. Surprisingly, C_4H_2 then increases toward the NPSV where some of the highest abundances are obtained in Figure 17h. This is unlikely to be a circulation effect, as C_4H_2 has only a slightly shorter loss timescale than C_3H_4 (Guerlet et al., 2010), so we might expect to see the same structure in C_3H_4. Photolysis of C_2H_2 is the dominant production mechanism for C_4H_2 (Moses et al., 2005), so the polar C_4H_2 may simply be a result of the excess C_2H_2 within the NPSV at high altitudes in Figure 16, which is not captured by the photochemical models. Conversely, C_3H_4 is primarily formed from interconversion of other C_3 hydrocarbons (Moses et al., 2005), which do not display the same enrichment as C_2H_2. Furthermore, the model of Moses and Greathouse (2005) overestimates equatorial C_3H_4 and C_4H_2 by factors of ∼5 and ∼4, respectively, similar to that found by Guerlet et al. (2010).

Methyl (CH_3, first detected by ISO, Bézard et al., 1998) is also a short-lived species produced directly from methane photolysis (Moses et al., 2000). MIRI/MRS provides the first latitudinally resolved measurements of CH_3, showing the same equator-to-pole decline as C_2H_2 and C_3H_4, along with a local minimum near 30°N that may be related to the seasonal upwelling. The seasonal model underpredicts the equatorial abundances by ∼2.5. Unlike most other hydrocarbon species, CH_3 appears to be most depleted within the NPSV, by a factor of ∼5 compared to equatorial abundances. This may reflect the annual-average insolation, with less CH_4 photolysis at the highest latitudes, although we note that methyl-methyl recombination reactions are dominant producer of C_2H_6, so it may have been mostly converted into the enriched ethane of the NPSV. Alternatively, we note that the CH_3 abundance is very sensitive to the methane homopause pressure (Bézard et al., 1998), so the CH_3 depletion in the NPSV could potentially be caused by subsidence through the upper stratosphere and lower thermosphere that pushes the methane homopause to deeper pressures, providing a consistent picture with the enhanced C_2H_4, C_2H_6, and some other hydrocarbon abundances.

Benzene (C_6H_6, first detected by Bézard et al. (2001a)) also differs substantially from neutral photochemical predictions, which would expect a distribution similar to that of C_2H_2. Instead, we see the C_6H_6 emission at all latitudes (e.g., between strong C_2H_2 lines in Figure 12), with enhancement by 1.5–2.0× within the NPSV compared to mid-latitudes. A similar latitudinal gradient was observed by Cassini/CIRS in the southern hemisphere between 2007 and 2012, with a slight enhancement within the SPSV (Guerlet et al., 2015). Nevertheless, the peak abundance at 0.5 mbar remains 50× smaller than the photochemical model prediction of Moses and Greathouse (2005), as previously found by Guerlet et al. (2015), and some 10× smaller than the coupled ion-neutral chemistry of Moses et al. (2023). As discussed by Koskinen et al. (2016) and Moses et al. (2023), benzene on Saturn is greatly enhanced by ion chemistry, and increased production due to auroral-induced ion chemistry may play a role at high latitudes, but finding a specific match between models and data remains a challenge.

It is interesting to note that, of all the hydrocarbon species observed by MIRI in 2022, none of them show the substantial chemical consequences predicted by neutral photochemistry (Moses et al., 2023) if the large influx of organic-rich ring material detected by Cassini during its Grand Finale in 2017 (Serigano et al., 2022) were vaporized/ablated upon entry into the equatorial stratosphere. Furthermore, no new nitriles were observed in 2022 (see below). We thus favor the hypothesis of Moses et al. (2023) that the ring material enters as small dust particles that do not ablate and affect the stratospheric composition.

5.4.4. Exogenic Species

Carbon dioxide (CO_2, first detected by ISO, Feuchtgruber et al., 1997) is detected at all latitudes by MIRI/MRS, with a relatively uniform abundance with latitude (0.60 ± 0.05 ppb at 0.5 mbar, Figure 17e) and hints of a slightly lower abundance (0.56 ± 0.03 ppb) within the NPSV. The distribution is approximately consistent with the few measurements available from Cassini (Abbas et al., 2013), but is inconsistent with photochemical models that assume a globally constant flux of incoming oxygen species and predict CO_2 abundances that are greatest near the equator and tail off toward high latitudes (Moses & Greathouse, 2005). There are no strong latitudinal gradients that might imply a spatially localized source (e.g., recent comets, Cavalié et al., 2010), or Enceladus plume and

ring material entering at specific latitudes, but icy grain ablation remains too small a source to explain the measurements (Moses & Poppe, 2017). Indeed, the uniform CO_2 distribution derived here does not match the exogenic H_2O distribution derived from Herschel observations, which showed enhancements at low latitudes (Cavalié et al., 2019). More work is required to robustly compare the CO_2 and H_2O distributions to elucidate their sources.

Unless Saturn suffers a large-scale impact event, or the equatorial ring influx does provide excess nitrile production (Moses et al., 2023), HCN is not an expected photochemical product on Saturn, as the regions of photolytic destruction of CH_4 and NH_3 are separated by hundreds of kilometres in the vertical. Any detection of the 14.04 μm (ν_2) HCN line is challenging due to blending with lines of C_2H_2. We also note that the MRS wavelength calibration (Argyriou et al., 2023) and spectral resolution (Jones et al., 2023) creates fitting artifacts in channel 3B, preventing a rigorous study of upper limits in this preliminary study. Nevertheless, we find that the MRS data support HCN abundances no larger than 1 ppb at $p < 1$ mbar, an improvement over the previous upper limit of 22 ppb at $p < 1$ mbar in the sub-millimeter from Herschel/SPIRE (Fletcher et al., 2012). We do not see any evidence of the ν_5 band of HC_3N at 15.08 μm, again confirming an absence of nitriles related to ring influx (Moses et al., 2023).

6. Conclusions

This initial survey of JWST/MIRI observations of Saturn has revealed a wealth of new insights into the evolution of the seasonal atmosphere during northern summer (November 2022, $L_s = 150°$); demonstrated MIRI/MRS capabilities to observe extended, bright, rotating, and moving planetary objects that are much larger than the fields-of-view; and provided a means to evaluate and mitigate challenges related to wavelength calibration, detector saturation, and instrumental artifacts for MIRI/MRS. Spatially resolved 4.9–27.9 μm maps of Saturn (three tiles spanning from the equator to the north pole) have been inverted to study the zonal-mean temperatures, windshears, aerosols, and gaseous composition from the cloud-forming region of the troposphere into the mid-stratosphere. This includes the first maps of the transitional region of Saturn's spectrum between 5.1 and 6.9 μm, where both thermal emission and scattered sunlight shape the spectrum, which were inaccessible to the VIMS and CIRS instruments on Cassini.

Although the JWST data reduction pipeline continues to evolve, we have presented algorithms for correcting artifacts such as wavelength calibration offsets, correction of partially saturated spectral regions, and the development of "flat-field" corrections by exploiting multiple dithers on the same target. As the MIRI/MRS spectral cubes required significant processing outside of the pipeline, we perform customized cleaning on each tile and dither independently, to prevent the blending of artifacts that, in the most extreme cases, can completely obscure the spatial structure of Saturn itself. With these artifacts removed, we summarize the initial survey of Saturn as follows:

1. *Saturn's banded structure*: Latitudinal gradients in temperatures and windshears show strong correlations with the locations of Saturn's mid-latitude eastward and westward jets (García-Melendo et al., 2011), with the contrasts between cool zones and warmer belts confirming the decay of the zonal winds with altitude via the thermal windshear equation. Conversely, gradients in reflectivity (and the derived aerosol structure from 4.9 to 7.3 μm) show similarities to albedo contrasts in observations acquired by Hubble in September 2022 (Simon et al., 2023), with a decrease in aerosols in distinct steps from equator to pole, with the highest cloud base and thickest tropospheric hazes within the broad reflective band equatorward of 15°N. A narrow equatorial band (<5°N) is dark at 5 μm, coinciding with the location where the narrow upper-tropospheric jet was previously detected (García-Melendo et al., 2011). The 5-μm brightness has evolved with time, such that a pole-encircling band from 62° to 78°N is now the brightest on the planet, coinciding with a dearth of aerosol opacity, whereas the polar domain (interior to the hexagon) is the darkest at 5 μm due to an absence of upper-tropospheric aerosols and an optically thick and compact cloud at higher pressures. We no longer see the 5-μm-bright, aerosol-depleted band near 35°–40°N that had dominated the appearance of the northern hemisphere after the 2010–2011 storm, consistent with a re-population of the band by Saturn's seasonal aerosols in the decade since the storm.

2. *NPSV*: The seasonal stratospheric vortex that developed poleward of 78°N during northern spring (Fletcher et al., 2018b) remained present in 2022, with warmer temperatures than those measured in 2017, now approaching the same temperatures as those observed in the SPSV during southern summer (2004–2005). Radiative models (e.g., Guerlet et al., 2014), combined with our Earth-based vantage point (Blake et al., 2022), suggest that the visibility of the warm NPSV will decline substantially in the next 1–2 years before autumn equinox. The sharp thermal gradient at the edge of the NPSV promotes negative windshear, and thus westward stratospheric winds entraining the NPSV for $p < 10$ mbar. MIRI/MRS did not detect evidence of the vertices of

Saturn's hexagon, meaning that we will need to wait until the 2040s for our next infrared views of the hexagon. However, the bright NPC was still visible, embedded within the NPSV. The NPSV was enriched in several stratospheric hydrocarbon species (ethane, acetylene, ethylene, benzene, diacetylene) due to a combination of polar subsidence over the summer pole, and potential ion-neutral chemistry at high latitudes.

3. *Cyclones and anticyclones*: Channel 1-short of MIRI/MRS offers the best opportunity to probe the fine-scale cloud banding, as well as discrete features. We observe contrasts associated with cyclones (bright and aerosol-free) and anticyclones (dark and cloudy) near 48°, 10°, and 62°N, but these could not be identified in contemporaneous amateur observations, nor Hubble observations ∼7 weeks earlier. This strongly argues for near-simultaneous MIRI/MRS spectroscopy and NIRCAM (or Hubble) imaging in future observing programs, alongside long-term records of variability from ground-based facilities.

4. *Saturn's Equatorial Stratospheric Oscillation*: Windshears derived from retrieved temperature gradients reveal diagonally stacked shear zones that rise to higher altitudes with higher latitudes, connecting the stratosphere throughout the low-latitudes equatorward of 30°N. MIRI/MRS reveals warm and cool temperature anomalies at the equator (and off-equatorial anomalies at 13°N) that are consistent with the downward propagation of the oscillatory pattern over a decade of pressure in the 5 years since the 2017 Cassini observations. A warm equatorial anomaly centred near 0.7 mbar is responsible for the bright equatorial band of emission observed in CH_4 and C_2H_2 emission, but this is opposite to the dark band observed from the ground one Saturnian year earlier (1993–1995, Blake et al., 2022; Orton et al., 2008), raising doubts about the semi-annual nature (i.e., 15-year period) of the equatorial oscillation. Thermal wind calculations imply the presence of an equatorial westward jet near 1–5 mbar in 2022 superimposed onto a broader region of eastward flow, but future joint campaigns between JWST and ALMA are necessary to confirm the validity of the thermal winds derived here.

5. *Reversal of Saturn's interhemispheric stratospheric circulation*: MIRI/MRS observations in 2022 reveal cooler temperatures in the 10°–40°N domain compared to Cassini in 2017. This coincides with local minima in several hydrocarbon species in 2022 (notably C_2H_2, C_2H_6, C_4H_2, and CH_3), opposite to the local maxima detected by Cassini (Guerlet et al., 2009, 2010; Sylvestre et al., 2015). This adiabatic cooling and hydrocarbon-depleted air implies a transition from wintertime subsidence to summertime upwelling in the northern hemisphere, as part of the seasonal reversal of Saturn's interhemispheric stratospheric circulation (Bardet et al., 2022; Friedson & Moses, 2012).

6. *Stacked aerosol layers*: We present the first assessment of aerosol opacity in 5.1–6.8 μm range, requiring two aerosol layers to reproduce the thermal emission and reflected sunlight components. The *upper aerosol layer*, possibly a photochemically produced haze related to diphosphine (Ferris & Benson, 1980), is thickest, highest (near 200 mbar) and most extended at the equator, but deeper (300 mbar) and more compact at mid-latitudes, before becoming negligible poleward of 60°N. This layer is likely to be the same as that detected by Cassini/ISS (Roman et al., 2013), and coincides with a region of localized radiative heating detected by Cassini/CIRS (Fletcher et al., 2007). The *deeper aerosol layer*, possibly associated with condensates of NH_3 and other species, resides at 1–2 bars, being shallowest (1.2 bars) near 10°N and deepest (2.6 bars) and most compact in the polar domain, responsible for both the dark thermal emission at 5 μm and the absence of reflectivity at 5.2 μm. Aerosol fitting for MIRI/MRS is somewhat degenerate, and further constraints could be provided in future by NIRSpec observations of reflected sunlight.

7. *Tropospheric species*: Latitudinal variability of *phosphine* appears to be most confined to $p < 1$ bar, displaying an equatorial maximum (Fletcher, Orton, Teanby, & Irwin, 2009) and general decline in abundance toward the polar domain. Regions of higher aerosol opacity generally correspond to regions of elevated PH_3, suggesting this disequilibrium species is most abundant when aerosols shield the molecule from photolysis. *Ammonia* displays a strong equatorial enrichment <5° of the equator (450–650 ppm), similar to the NH_3-enriched column in Jupiter's equatorial zone (Achterberg et al., 2006; de Pater et al., 2016; Li et al., 2017) and suggesting similar dynamical processes at the equators of both gas giants. NH_3 also displays different latitudinal distributions above and below the condensed aerosols near 1.7 bars, suggestive of differing circulation patterns at different heights. Neither PH_3 nor NH_3 display consistent belt/zone contrasts at mid-latitudes, suggesting secondary circulation patterns associated with mid-latitude Ferrel cells may be weak. Tropospheric *water* is mapped for the first time in its condensation region (i.e., above the expected H_2O cloud), with estimates at 3.3 bars varying from 200 ppb at the equator to 10 ppb near 5°N, and a distinct step in the abundance near ∼40°N from 145 at low latitudes to 80 ppb at higher latitudes.

8. *Stratospheric chemicals*: Short-lived hydrocarbons, such as *acetylene*, *diacetylene*, *methylacetylene*, *ethylene*, *and methyl*, tend to track the annual-average insolation (i.e., peaking at low latitudes, consistent with the

predictions of seasonal photochemical models, Moses & Greathouse, 2005), whereas longer-lived species (*ethane*, *propane*, *and possibly benzene*) appear to be more influenced by long-term stratospheric circulation redistributing gases to higher latitudes. Acetylene has a steeper vertical gradient within the NPSV than elsewhere, and several species (ethane, ethylene, benzene, diacetylene) show strong enrichments within the NPSV. Methyl is mapped with latitude for the first time, showing a factor of ∼5 decrease from equator to pole. Ethylene is detected in the NPSV for the first time. The benzene abundance remains an order of magnitude smaller than the predictions of photochemical models. *Carbon dioxide* is detected at all latitudes with a relatively uniform distribution, lacking strong latitudinal gradients that might imply a spatially localized source of exogenic oxygen species.

9. *Absence of nitriles*: None of the hydrocarbon distributions support the substantial chemical consequences predicted by neutral photochemistry (Moses et al., 2023) if the large influx of ring material detected by Cassini in 2017 (Serigano et al., 2022) were vaporized upon entry into the equatorial stratosphere. Neither HCN nor HC_3N, both predicted by nitrile chemistry related to ring influx, are detected by MIRI. This suggests that ring material influx is not strongly influencing Saturn's equatorial stratosphere.

We caution the reader that the MIRI/MRS calibration continues to evolve, and that refined cleaning techniques will enable future in depth studies - in particular, removal of instrument artifacts from the 17–28 μm domain will enable studies of temperature and para-H_2 at longer wavelengths; plus a more sensitive search for stratospheric emission lines throughout the MIRI spectrum. Future joint campaigns with other JWST instruments (NIRSpec and NIRCAM) would aid in breaking degeneracies in aerosol retrievals, and collaboration with ALMA would allow a direct comparison of stratospheric winds and thermal winds associated with equatorial and polar jets.

JWST observations of the Saturn system in November 2022 ($L_s = 150°$) have revealed the wealth of possibilities offered by IFU spectroscopy from space in the mid-infrared. But Saturn's atmosphere will continue to change with the onset of northern autumn (May 2025, $L_s = 180°$), and we hope that these Cycle-1 observations will mark the starting point for a long-term MIRI legacy program to track the seasonal evolution of Saturn's circulation and chemistry through to the next southern summer solstice (April 2032, $L_s = 270°$), completing the seasonal assessment begun by Cassini.

Data Availability Statement

Level-3 calibrated Saturn MIRI/MRS data from the standard pipeline are available directly from the MAST archive (MAST Archive, 2022). Hubble observations used for comparison were acquired by the Outer Planets Legacy Program (OPAL Archive, 2022).

The NEMESIS radiative transfer and retrieval code (Irwin et al., 2008) used in this study is open-access and is available for download (Irwin, 2022).

The JWST calibration pipeline is available via Bushouse et al. (2023), this work used version 1.9.4.

The custom pipeline and data processing code developed in this study is available at King et al. (2023).

The data products produced in this study, including synthetic flat fields, zonal average spectra and quick-look visualizations, are available from Fletcher (2023).

References

Abbas, M. M., LeClair, A., Woodard, E., Young, M., Stanbro, M., Flasar, F. M., et al. (2013). Distribution of CO_2 in Saturn's atmosphere from Cassini/CIRS infrared observations. *The Astrophysical Journal*, 776(2), 73. https://doi.org/10.1088/0004-637X/776/2/73

Achterberg, R. K., Conrath, B. J., & Gierasch, P. J. (2006). Cassini CIRS retrievals of ammonia in Jupiter's upper troposphere. *Icarus*, 182(1), 169–180. https://doi.org/10.1016/j.icarus.2005.12.020

Adam, A. Y., Yachmenev, A., Yurchenko, S. N., & Jensen, P. (2019). Variationally computed IR line list for the methyl radical CH_3. *Journal of Physical Chemistry A*, 123(22), 4755–4763. https://doi.org/10.1021/acs.jpca.9b02919

Argyriou, I., Glasse, A., Law, D. R., Labiano, A., Álvarez-Márquez, J., Patapis, P., et al. (2023). JWST MIRI flight performance: The Medium-Resolution Spectrometer. arXiv e-prints, arXiv:2303.13469. https://doi.org/10.48550/arXiv.2303.13469

Bailly, D., Birnbaum, G., Buechele, A., Flaud, P. M., & Hartmann, J. M. (2004). Absorption by pure NH_3 and NH_3-H_2 mixtures in the 5 μm window region. *Journal of Quantitative Spectroscopy and Radiative Transfer*, 83, 1–13. https://doi.org/10.1016/S0022-4073(02)00281-9

Baines, K. H., Drossart, P., Momary, T. W., Formisano, V., Griffith, C., Bellucci, G., et al. (2006). The atmospheres of Saturn and Titan in the near-infrared: First results of Cassini/VIMS. *Earth, Moon, and Planets*, 96(3–4), 1–29. https://doi.org/10.1007/s11038-005-9058-2

Bardet, D., Spiga, A., & Guerlet, S. (2022). Joint evolution of equatorial oscillation and interhemispheric circulation in Saturn's stratosphere. *Nature Astronomy*, 6(7), 804–811. https://doi.org/10.1038/s41550-022-01670-7

Benmahi, B., Cavalié, T., Fouchet, T., Moreno, R., Lellouch, E., Bardet, D., et al. (2022). First absolute wind measurements in Saturn's stratosphere from ALMA observations. *Astronomy and Astrophysics*, 666, A117. https://doi.org/10.1051/0004-6361/202244200

Bézard, B., Drossart, P., Encrenaz, T., & Feuchtgruber, H. (2001a). Benzene on the giant planets. *Icarus*, *154*(2), 492–500. https://doi.org/10.1006/icar.2001.6719

Bézard, B., Feuchtgruber, H., Moses, J. I., & Encrenaz, T. (1998). Detection of methyl radicals (CH_3) on Saturn. *Astronomy and Astrophysics*, *334*, L41–L44.

Bézard, B., Moses, J. I., Lacy, J., Greathouse, T., Richter, M., & Griffith, C. (2001b). Detection of ethylene (C_2H_4) on Jupiter and Saturn in non-auroral regions. In *Bulletin of the american astronomical society* (p. 1079).

Bjoraker, G., Wong, M., Hewagama, T., Orton, G., & Momary, T. (2020). The evolution of deep clouds on Saturn using 5-micron observations. In *Aas/division for planetary sciences meeting abstracts* (Vol. 52, p. 201-03).

Blake, J. S. D., Fletcher, L. N., Orton, G. S., Antunano, A., Roman, M. T., Kasaba, Y., et al. (2022). Saturn's seasonal variability from four decades of ground-based mid-infrared observations. *Icarus*, *392*, 115347. https://doi.org/10.1016/j.icarus.2022.115347

Bushouse, H., Eisenhamer, J., Dencheva, N., Davies, J., Greenfield, P., Morrison, J., et al. (2023). JWST calibration pipeline [Software]. https://doi.org/10.5281/zenodo.7038885

Caldwell, J., Hua, X.-M., Turgeon, B., Westphal, J. A., & Barnet, C. D. (1993). The drift of Saturn's north polar SPOT observed by the Hubble Space Telescope. *Science*, *260*(5106), 326–329. https://doi.org/10.1126/science.260.5106.326

Cavalié, T., Hartogh, P., Billebaud, F., Dobrijevic, M., Fouchet, T., Lellouch, E., et al. (2010). A cometary origin for CO in the stratosphere of Saturn? *Astronomy and Astrophysics*, *510*, A88. https://doi.org/10.1051/0004-6361/200912909

Cavalié, T., Hue, V., Hartogh, P., Moreno, R., Lellouch, E., Feuchtgruber, H., et al. (2019). Herschel map of Saturn's stratospheric water, delivered by the plumes of Enceladus. *Astronomy and Astrophysics*, *630*, A87. https://doi.org/10.1051/0004-6361/201935954

Coles, P. A., Yurchenko, S. N., Kovacich, R. P., Hobby, J., & Tennyson, J. (2019). A variationally computed room temperature line list for AsH_3. *Physical Chemistry Chemical Physics*, *21*(6), 3264–3277. https://doi.org/10.1039/C8CP07110A

Conrath, B. J., & Gautier, D. (2000). Saturn Helium abundance: A reanalysis of Voyager measurements. *Icarus*, *144*(1), 124–134. https://doi.org/10.1006/icar.1999.6265

Conrath, B. J., & Pirraglia, J. A. (1983). Thermal structure of Saturn from Voyager infrared measurements - Implications for atmospheric dynamics. *Icarus*, *53*(2), 286–292. https://doi.org/10.1016/0019-1035(83)90148-3

de Graauw, T., Feuchtgruber, H., Bézard, B., Drossart, P., Encrenaz, T., Beintema, D. A., et al. (1997). First results of ISO-SWS observations of Saturn: Detection of CO_2, CH_3C_2H, C_4H_2 and tropospheric H_2O. *Astronomy and Astrophysics*, *321*, L13–L16.

Delahaye, T., Armante, R., Scott, N. A., Jacquinet-Husson, N., Chédin, A., Crépeau, L., et al. (2021). The 2020 edition of the GEISA spectroscopic database. *Journal of Molecular Spectroscopy*, *380*, 111510. https://doi.org/10.1016/j.jms.2021.111510

Del Genio, A. D., Achterberg, R. K., Baines, K. H., Flasar, F. M., Read, P. L., Sánchez-Lavega, A., & Showman, A. P. (2009). Saturn atmospheric structure and dynamics, in: Saturn from Cassini-Huygens. In M. K. Dougherty, L. W. Esposito, & S. M. Krimigis (Eds.), *Saturn from Cassini-Huygens* (pp. 113–159). Springer. https://doi.org/10.1007/978-1-4020-9217-6_6

del Río-Gaztelurrutia, T., Sánchez-Lavega, A., Antuñano, A., Legarreta, J., García-Melendo, E., Sayanagi, K. M., et al. (2018). A planetary-scale disturbance in a long living three vortex coupled system in Saturn's atmosphere. *Icarus*, *302*, 499–513. https://doi.org/10.1016/j.icarus.2017.11.029

de Pater, I., Sault, R. J., Butler, B., DeBoer, D., & Wong, M. H. (2016). Peering through Jupiter's clouds with radio spectral imaging. *Science*, *352*(6290), 1198–1201. https://doi.org/10.1126/science.aaf2210

Encrenaz, T. (2003). ISO observations of the giant planets and Titan: What have we learnt? *Planetary and Space Science*, *51*(2), 89–103. https://doi.org/10.1016/S0032-0633(02)00145-9

Ferris, J. P., & Benson, R. (1980). Diphosphine is an intermediate in the photolysis of phosphine to phosphorus and hydrogen. *Nature*, *285*(5761), 156–157. https://doi.org/10.1038/285156a0

Feuchtgruber, H., Lellouch, E., de Graauw, T., Bezard, B., Encrenaz, T., & Griffin, M. (1997). External supply of oxygen to the atmospheres of giant planets. *Nature*, *389*(6647), 159–162. https://doi.org/10.1038/38236

Fletcher, L. N. (2023). Supporting data for JWST saturn atmosphere [Dataset]. https://doi.org/10.5281/zenodo.7891588

Fletcher, L. N., Baines, K. H., Momary, T. W., Showman, A. P., Irwin, P. G. J., Orton, G. S., et al. (2011). Saturn's tropospheric composition and clouds from Cassini/VIMS 4.6-5.1 µm nightside spectroscopy. *Icarus*, *214*(2), 510–533. https://doi.org/10.1016/j.icarus.2011.06.006

Fletcher, L. N., Guerlet, S., Orton, G. S., Cosentino, R. G., Fouchet, T., Irwin, P. G. J., et al. (2017). Disruption of Saturn's quasi-periodic equatorial oscillation by the great northern storm. *Nature Astronomy*, *1*(11), 765–770. https://doi.org/10.1038/s41550-017-0271-5

Fletcher, L. N., Gustafsson, M., & Orton, G. S. (2018a). Hydrogen dimers in giant-planet infrared spectra. *Astrophysical Journal Supplement Series*, *235*(1), 24. https://doi.org/10.3847/1538-4365/aaa07a

Fletcher, L. N., Hammel, H., Milam, S., de Pater, I., Fouchet, T., Orton, G., et al. (2021). The JWST giant planet atmospheres programme. In *European planetary science congress*. https://doi.org/10.5194/epsc2021-39

Fletcher, L. N., Irwin, P. G. J., Achterberg, R. K., Orton, G. S., & Flasar, F. M. (2016). Seasonal variability of Saturn's tropospheric temperatures, winds and para-H_2 from Cassini far-IR spectroscopy. *Icarus*, *264*, 137–159. https://doi.org/10.1016/j.icarus.2015.09.009

Fletcher, L. N., Irwin, P. G. J., Orton, G. S., Teanby, N. A., Achterberg, R. K., Bjoraker, G. L., et al. (2008). Temperature and composition of Saturn's polar hot spots and hexagon. *Science*, *319*(5859), 79–82. https://doi.org/10.1126/science.1149514

Fletcher, L. N., Irwin, P. G. J., Teanby, N. A., Orton, G. S., Parrish, P. D., Calcutt, S. B., et al. (2007). Characterising Saturn's vertical temperature structure from Cassini/CIRS. *Icarus*, *189*(2), 457–478. https://doi.org/10.1016/j.icarus.2007.02.006

Fletcher, L. N., Kaspi, Y., Guillot, T., & Showman, A. P. (2020a). How well do we understand the belt/zone circulation of giant planet atmospheres? *Space Science Reviews*, *216*(2), 30. https://doi.org/10.1007/s11214-019-0631-9

Fletcher, L. N., Orton, G. S., Sinclair, J. A., Guerlet, S., Read, P. L., Antuñano, A., et al. (2018b). A hexagon in Saturn's northern stratosphere surrounding the emerging summertime polar vortex. *Nature Communications*, *9*(1), 3564. https://doi.org/10.1038/s41467-018-06017-3

Fletcher, L. N., Orton, G. S., Teanby, N. A., & Irwin, P. G. J. (2009). Phosphine on Jupiter and Saturn from Cassini/CIRS. *Icarus*, *202*(2), 543–564. https://doi.org/10.1016/j.icarus.2009.03.023

Fletcher, L. N., Orton, G. S., Teanby, N. A., Irwin, P. G. J., & Bjoraker, G. L. (2009). Methane and its isotopologues on Saturn from Cassini/CIRS observations. *Icarus*, *199*(2), 351–367. https://doi.org/10.1016/j.icarus.2008.09.019

Fletcher, L. N., Sromovsky, L., Hue, V., Moses, J. I., Guerlet, S., West, R. A., & Koskinen, T. (2020b). Saturn's seasonal atmosphere at northern summer solstice. arXiv e-prints, arXiv:2012.09288.

Fletcher, L. N., Swinyard, B., Salji, C., Polehampton, E., Fulton, T., Sidher, S., et al. (2012). Sub-millimetre spectroscopy of Saturn's trace gases from Herschel/SPIRE. *Astronomy and Astrophysics*, *539*, A44. https://doi.org/10.1051/0004-6361/201118415

Fouchet, T., Guerlet, S., Strobel, D., Simon-Miller, A., Bézard, B., & Flasar, F. (2008). An equatorial oscillation in Saturn's middle atmosphere. *Nature*, *453*(7192), 200–202. https://doi.org/10.1038/nature06912

Friedson, A. J., & Moses, J. I. (2012). General circulation and transport in Saturn's upper troposphere and stratosphere. *Icarus*, *218*(2), 861–875. https://doi.org/10.1016/j.icarus.2012.02.004

García-Melendo, E., Pérez-Hoyos, S., Sánchez-Lavega, A., & Hueso, R. (2011). Saturn's zonal wind profile in 2004–2009 from Cassini ISS images and its long-term variability. *Icarus*, *215*(1), 62–74. https://doi.org/10.1016/j.icarus.2011.07.005

Gardner, J. P., Mather, J. C., Abbott, R., Abell, J. S., Abernathy, M., Abney, F. E., et al. (2023). The James Webb space telescope mission. *Publications of the Astronomical Society of the Pacific*, *135*(1048), 068001. https://doi.org/10.48550/arXiv.2304.04869

Giles, R. S., Fletcher, L. N., & Irwin, P. G. J. (2015). Cloud structure and composition of Jupiter's troposphere from 5- µm Cassini VIMS spectroscopy. *Icarus*, *257*, 457–470. https://doi.org/10.1016/j.icarus.2015.05.030

Gordon, I. E., Rothman, L. S., Hargreaves, R. J., Hashemi, R., Karlovets, E. V., Skinner, F. M., et al. (2022). The HITRAN2020 molecular spectroscopic database. *Journal of Quantitative Spectroscopy and Radiative Transfer*, *277*, 107949. https://doi.org/10.1016/j.jqsrt.2021.107949

Guerlet, S., Fouchet, T., Bézard, B., Moses, J. I., Fletcher, L. N., Simon-Miller, A. A., & Michael Flasar, F. (2010). Meridional distribution of CH_3C_2H and C_4H_2 in Saturn's stratosphere from CIRS/Cassini limb and nadir observations. *Icarus*, *209*(2), 682–695. https://doi.org/10.1016/j.icarus.2010.03.033

Guerlet, S., Fouchet, T., Bézard, B., Simon-Miller, A. A., & Flasar, F. M. (2009). Vertical and meridional distribution of ethane, acetylene and propane in Saturn's stratosphere from CIRS/Cassini limb observations. *Icarus*, *203*(1), 214–232. https://doi.org/10.1016/j.icarus.2009.04.002

Guerlet, S., Fouchet, T., Vinatier, S., Simon, A. A., Dartois, E., & Spiga, A. (2015). Stratospheric benzene and hydrocarbon aerosols detected in Saturn's auroral regions. *Astronomy & Astrophysics*, *580*, A89. https://doi.org/10.1051/0004-6361/201424745

Guerlet, S., Spiga, A., Sylvestre, M., Indurain, M., Fouchet, T., Leconte, J., et al. (2014). Global climate modeling of Saturn's atmosphere. Part I: Evaluation of the radiative transfer model. *Icarus*, *238*, 110–124. https://doi.org/10.1016/j.icarus.2014.05.010

Hesman, B. E., Bjoraker, G. L., Sada, P. V., Achterberg, R. K., Jennings, D. E., Romani, P. N., et al. (2012). Elusive ethylene detected in Saturn's northern storm region. *The Astrophysical Journal*, *760*(1), 24. https://doi.org/10.1088/0004-637X/760/1/24

Holton, J. (2004). *An introduction to dynamic meteorology*. Academic Press.

Howett, C. J. A., Carlson, R. W., Irwin, P. G. J., & Calcutt, S. B. (2007). Optical constants of ammonium hydrosulfide ice and ammonia ice. *Journal of the Optical Society of America B: Optical Physics*, *24*(1), 126–136. https://doi.org/10.1364/JOSAB.24.000126

Hue, V., Cavalié, T., Dobrijevic, M., Hersant, F., & Greathouse, T. K. (2015). 2D photochemical modeling of Saturn's stratosphere. Part I: Seasonal variation of atmospheric composition without meridional transport. *Icarus*, *257*, 163–184. https://doi.org/10.1016/j.icarus.2015.04.001

Hue, V., Greathouse, T. K., Cavalié, T., Dobrijevic, M., & Hersant, F. (2016). 2D photochemical modeling of Saturn's stratosphere. Part II: Feedback between composition and temperature. *Icarus*, *267*, 334–343. https://doi.org/10.1016/j.icarus.2015.12.007

Hueso, R., Juaristi, J., Legarreta, J., Sánchez-Lavega, A., Rojas, J. F., Erard, S., et al. (2018). The planetary virtual observatory and laboratory (PVOL) and its integration into the Virtual European Solar and Planetary Access (VESPA). *Planetary and Space Science*, *150*, 22–35. https://doi.org/10.1016/j.pss.2017.03.014

Hurley, J., Fletcher, L. N., Irwin, P. G. J., Calcutt, S. B., Sinclair, J. A., & Merlet, C. (2012). Latitudinal variation of upper tropospheric NH_3 on Saturn derived from Cassini/CIRS far-infrared measurements. *Planetary and Space Science*, *73*(1), 347–363. https://doi.org/10.1016/j.pss.2012.08.003

Irwin, P. G. J. (2022). NEMESIS retrieval code [Software]. https://doi.org/10.5281/zenodo.5816724

Irwin, P. G. J., Teanby, N. A., de Kok, R., Fletcher, L., Howett, C., Tsang, C., et al. (2008). The NEMESIS planetary atmosphere radiative transfer and retrieval tool. *Journal of Quantitative Spectroscopy and Radiative Transfer*, *109*(6), 1136–1150. https://doi.org/10.1016/j.jqsrt.2007.11.006

Irwin, P. G. J., Teanby, N. A., Fletcher, L. N., Toledo, D., Orton, G. S., Wong, M. H., et al. (2022). Hazy blue worlds: A Holistic aerosol model for Uranus and Neptune, including dark spots. *Journal of Geophysical Research: Planets*, *127*(6), e07189. https://doi.org/10.1029/2022JE007189

Jones, O. C., Álvarez-Márquez, J., Sloan, G. C., Kavanagh, P. J., Argyriou, I., Labiano, A., et al. (2023). Observations of the planetary Nebula SMP LMC 058 with the JWST MIRI medium resolution spectrometer. *Monthly Notices of the Royal Astronomical Society*, *523*(2), 2519–2529. https://doi.org/10.48550/arXiv.2301.13233

Karkoschka, E., & Tomasko, M. G. (1993). Saturn's upper atmospheric hazes observed by the Hubble Space Telescope. *Icarus*, *106*(2), 428–441. https://doi.org/10.1006/icar.1993.1183

King, O. R., Harkett, J., Fletcher, L. N., & Melin, H. (2023). Custom JWST/MIRI processing pipeline [Software]. https://doi.org/10.5281/zenodo.7891560

Koskinen, T. T., Moses, J. I., West, R. A., Guerlet, S., & Jouchoux, A. (2016). The detection of benzene in Saturn's upper atmosphere. *Geophysical Research Letters*, *43*(15), 7895–7901. https://doi.org/10.1002/2016GL070000

Labiano, A., Argyriou, I., Álvarez-Márquez, J., Glasse, A., Glauser, A., Patapis, P., et al. (2021). Wavelength calibration and resolving power of the JWST MIRI medium resolution spectrometer. *Astronomy and Astrophysics*, *656*, A57. https://doi.org/10.1051/0004-6361/202140614

Laraia, A. L., Ingersoll, A. P., Janssen, M. A., Gulkis, S., Oyafuso, F., & Allison, M. (2013). Analysis of Saturn's thermal emission at 2.2-cm wavelength: Spatial distribution of ammonia vapor. *Icarus*, *226*(1), 641–654. https://doi.org/10.1016/j.icarus.2013.06.017

Li, C., Ingersoll, A., Janssen, M., Levin, S., Bolton, S., Adumitroaie, V., et al. (2017). The distribution of ammonia on Jupiter from a preliminary inversion of Juno microwave radiometer data. *Geophysical Research Letters*, *44*(11), 5317–5325. https://doi.org/10.1002/2017GL073159

Martonchik, J. V., Orton, G. S., & Appleby, J. F. (1984). Optical properties of NH_3 ice from the far infrared to the near ultraviolet. *Applied Optics*, *23*(4), 541–547. https://doi.org/10.1364/ao.23.000541

MAST Archive. (2022). JWST MIRI/MRS saturn observations 1247 [Data]. https://doi.org/10.17909/wjpz-7383

Moses, J. I., Armstrong, E. S., Fletcher, L. N., Friedson, A. J., Irwin, P. G. J., Sinclair, J. A., & Hesman, B. E. (2015). Evolution of stratospheric chemistry in the Saturn storm beacon region. *Icarus*, *261*, 149–168. https://doi.org/10.1016/j.icarus.2015.08.012

Moses, J. I., Bézard, B., Lellouch, E., Gladstone, G. R., Feuchtgruber, H., & Allen, M. (2000). Photochemistry of Saturn's atmosphere. I. Hydrocarbon chemistry and comparisons with ISO observations. *Icarus*, *143*(2), 244–298. https://doi.org/10.1006/icar.1999.6270

Moses, J. I., Brown, Z. L., Koskinen, T. T., Fletcher, L. N., Serigano, J., Guerlet, S., et al. (2023). Saturn's atmospheric response to the large influx of ring material inferred from Cassini INMS measurements. *Icarus*, *391*, 115328. https://doi.org/10.1016/j.icarus.2022.115328

Moses, J. I., Fouchet, T., Bézard, B., Gladstone, G. R., Lellouch, E., & Feuchtgruber, H. (2005). Photochemistry and diffusion in Jupiter's stratosphere: Constraints from ISO observations and comparisons with other giant planets. *Journal of Geophysical Research*, *110*(E8), E08001. https://doi.org/10.1029/2005JE002411

Moses, J. I., & Greathouse, T. K. (2005). Latitudinal and seasonal models of stratospheric photochemistry on Saturn: Comparison with infrared data from IRTF/TEXES. *Journal of Geophysical Research*, *110*(E9), E09007. https://doi.org/10.1029/2005JE002450

Moses, J. I., Liang, M.-C., Yung, Y. L., & Shia, R.-L. (2007). Two-dimensional photochemical modeling of hydrocarbon abundances on Saturn. In *Lunar and planetary science conference* (Vol. 38, p. 2196).

Moses, J. I., & Poppe, A. R. (2017). Dust ablation on the giant planets: Consequences for stratospheric photochemistry. *Icarus*, *297*, 33–58. https://doi.org/10.1016/j.icarus.2017.06.002

Noll, K. S., & Larson, H. P. (1990). The spectrum of saturn from 1990–2230 cm^{-1}: Abundances of AsH$_3$, CH$_3$D, CO, GeH$_4$, and PH$_3$. *Icarus*, *89*(1), 168–189. https://doi.org/10.1016/0019-1035(91)90096-c

OPAL Archive. (2022). Outer planets legacy program archive [Data]. https://doi.org/10.17909/T9G593

Orton, G., Yanamandra-Fisher, P., Fisher, B., Friedson, A., Parrish, P., Nelson, J., et al. (2008). Semi-annual oscillations in Saturn's low-latitude stratospheric temperatures. *Nature*, *453*(7192), 196–198. https://doi.org/10.1038/nature06897

Pérez-Hoyos, S., Sanz-Requena, J. F., Sánchez-Lavega, A., Irwin, P. G. J., & Smith, A. (2016). Saturn's tropospheric particles phase function and spatial distribution from Cassini ISS 2010-11 observations. *Icarus*, *277*, 1–18. https://doi.org/10.1016/j.icarus.2016.04.022

Pirraglia, J. A., Conrath, B. J., Allison, M. D., & Gierasch, P. J. (1981). Thermal structure and dynamics of saturn and Jupiter. *Nature*, *292*(5825), 677–679. https://doi.org/10.1038/292677a0

Read, P. L., Conrath, B. J., Fletcher, L. N., Gierasch, P. J., Simon-Miller, A. A., & Zuchowski, L. C. (2009). Mapping potential vorticity dynamics on Saturn: Zonal mean circulation from Cassini and Voyager data. *Planetary and Space Science*, *57*(14–15), 1682–1698. https://doi.org/10.1016/j.pss.2009.03.004

Roman, M. T., Banfield, D., & Gierasch, P. J. (2013). Saturn's cloud structure inferred from Cassini ISS. *Icarus*, *225*(1), 93–110. https://doi.org/10.1016/j.icarus.2013.03.015

Sánchez-Lavega, A., García-Muñoz, A., del Río-Gaztelurrutia, T., Pérez-Hoyos, S., Sanz-Requena, J. F., Hueso, R., et al. (2020). Multilayer hazes over Saturn's hexagon from Cassini ISS limb images. *Nature Communications*, *11*(1), 2281. https://doi.org/10.1038/s41467-020-16110-1

Sayanagi, K. M., Dyudina, U. A., Ewald, S. P., Fischer, G., Ingersoll, A. P., Kurth, W. S., et al. (2013). Dynamics of Saturn's great storm of 2010–2011 from Cassini ISS and RPWS. *Icarus*, *223*(1), 460–478. https://doi.org/10.1016/j.icarus.2012.12.013

Serigano, J., Hörst, S. M., He, C., Gautier, T., Yelle, R. V., Koskinen, T. T., et al. (2022). Compositional measurements of Saturn's upper atmosphere and rings from Cassini INMS: An extended analysis of measurements from Cassini's Grand Finale orbits. *Journal of Geophysical Research: Planets*, *127*(6), e07238. https://doi.org/10.1029/2022JE007238

Simon, A. A., Hedman, M. M., Nicholson, P. D., Tiscareno, M. S., Showalter, M. R., McDonald, T., & Callos, S. (2023). Hubble detects the start of a new saturn ring spoke season. *Geophysical Research Letters*, *50*(3), e2022GL101904. https://doi.org/10.1029/2022GL101904

Sinclair, J. A., Irwin, P. G. J., Fletcher, L. N., Moses, J. I., Greathouse, T. K., Friedson, A. J., et al. (2013). Seasonal variations of temperature, acetylene and ethane in Saturn's atmosphere from 2005 to 2010, as observed by Cassini-CIRS. *Icarus*, *225*(1), 257–271. https://doi.org/10.1016/j.icarus.2013.03.011

Sromovsky, L. A., Baines, K. H., & Fry, P. M. (2013). Saturn's Great Storm of 2010–2011: Evidence for ammonia and water ices from analysis of VIMS spectra. *Icarus*, *226*(1), 402–418. https://doi.org/10.1016/j.icarus.2013.05.043

Sromovsky, L. A., Baines, K. H., & Fry, P. M. (2021). Evolution of Saturn's north polar color and cloud structure between 2012 and 2017 inferred from Cassini VIMS and ISS observations. *Icarus*, *362*, 114409. https://doi.org/10.1016/j.icarus.2021.114409

Sromovsky, L. A., Baines, K. H., Fry, P. M., & Momary, T. W. (2016). Cloud clearing in the wake of Saturn's Great Storm of 2010–2011 and suggested new constraints on Saturn's He/H$_2$ ratio. *Icarus*, *276*, 141–162. https://doi.org/10.1016/j.icarus.2016.04.031

Stam, D. M., Banfield, D., Gierasch, P. J., Nicholson, P. D., & Matthews, K. (2001). Near-IR spectrophotometry of Saturnian aerosols-meridional and vertical distribution. *Icarus*, *152*(2), 407–422. https://doi.org/10.1006/icar.2001.6641

Sung, K., Toon, G. C., Mantz, A. W., & Smith, M. A. H. (2013). FT-IR measurements of cold C$_3$H$_8$ cross sections at 7–15 μm for Titan atmosphere. *Icarus*, *226*(2), 1499–1513. https://doi.org/10.1016/j.icarus.2013.07.028

Sylvestre, M., Guerlet, S., Fouchet, T., Spiga, A., Flasar, F. M., Hesman, B., & Bjoraker, G. L. (2015). Seasonal changes in Saturn's stratosphere inferred from Cassini/CIRS limb observations. *Icarus*, *258*, 224–238. https://doi.org/10.1016/j.icarus.2015.05.025

Tennyson, J., Yurchenko, S. N., Al-Refaie, A. F., Barton, E. J., Chubb, K. L., Coles, P. A., et al. (2016). The ExoMol database: Molecular line lists for exoplanet and other hot atmospheres. *Journal of Molecular Spectroscopy*, *327*, 73–94. https://doi.org/10.1016/j.jms.2016.05.002

Vasavada, A. R., & Showman, A. P. (2005). Jovian atmospheric dynamics: An update after Galileo and Cassini. *Reports on Progress in Physics*, *68*(8), 1935–1996. https://doi.org/10.1088/0034-4885/68/8/R06

Wells, M., Pel, J.-W., Glasse, A., Wright, G. S., Aitink-Kroes, G., Azzollini, R., et al. (2015). The mid-infrared instrument for the James Webb space telescope, VI: The medium resolution spectrometer. *Publications of the Astronomical Society of the Pacific*, *127*(953), 646–664. https://doi.org/10.1086/682281

Westphal, J. A., Baum, W. A., Ingersoll, A. P., Barnet, C. D., de Jong, E. M., Danielson, G. E., & Caldwell, J. (1992). Hubble Space Telescope observations of the 1990 equatorial disturbance on Saturn - Images, albedos, and limb darkening. *Icarus*, *100*(2), 485–498. https://doi.org/10.1016/0019-1035(92)90112-K

Wright, G. S., Rieke, G. H., Glasse, A., Ressler, M., Marín, M. G., Aguilar, J., et al. (2023). The mid-infrared instrument for JWST and its in-flight performance. *Publications of the Astronomical Society of the Pacific*, *135*(1046), 048003. https://doi.org/10.1088/1538-3873/acbe66

Yanamandra-Fisher, P. A., Orton, G. S., Fisher, B. M., & Sánchez-Lavega, A. (2001). NOTE: Saturn's 5.2-μm cold spots: Unexpected cloud variability. *Icarus*, *150*(1), 189–193. https://doi.org/10.1006/icar.2000.6580